iScience

CellPress
OPEN ACCESS

Article

The prion protein is required for normal responses to light stimuli by photoreceptors and bipolar cells

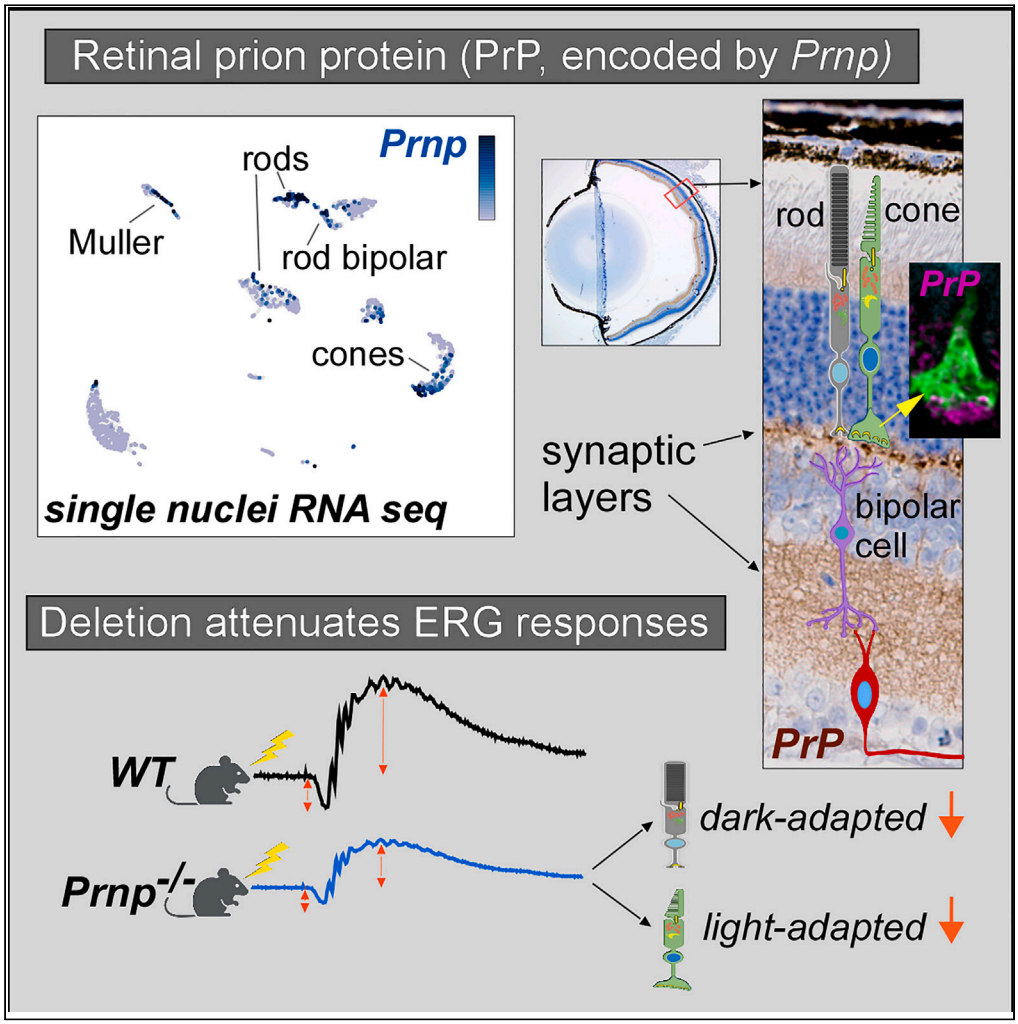

James F. Striebel, James A. Carroll, Brent Race, ..., Catherine Bowes Rickman, Bruce Chesebro, Mikael Klingeborn

striebelj@nih.gov (J.F.S.)
mikael@mclaughlinresearch.org (M.K.)

Highlights

In retina, photoreceptor cells show highest expression of *Prnp* transcripts

Prion protein (PrP^C) localizes to photoreceptor-bipolar cell synapses

Deletion of *Prnp* alters scotopic and photopic ERG responses

Normal synaptic structure in PrPKO mice suggests functional role for PrP^C

Striebel et al., iScience *27*, 110954
October 18, 2024 Published by Elsevier Inc.
https://doi.org/10.1016/j.isci.2024.110954

iScience

CellPress
OPEN ACCESS

Article

The prion protein is required for normal responses to light stimuli by photoreceptors and bipolar cells

James F. Striebel,[1,6,*] James A. Carroll,[1] Brent Race,[1] Jacqueline M. Leung,[2] Cindi Schwartz,[2] Emily D. Reese,[5] Catherine Bowes Rickman,[3,4] Bruce Chesebro,[1] and Mikael Klingeborn[3,5,*]

SUMMARY

The prion protein, PrP^C, is well known as an essential susceptibility factor for neurodegenerative prion diseases, yet its function in normal, healthy cells remains uncertain. A role in synaptic function has been proposed for PrP^C, supported by its cell surface expression in neurons and glia. Here, in mouse retina, we localized PrP^C to the junctions between photoreceptors and bipolar cells using synaptic proteins EAAT5, CtBP2, and PSD-95. PrP^C localized most densely with bipolar cell dendrites synapsing with cone photoreceptors. In two coisogenic mouse strains, deletion of the gene encoding PrP^C, *Prnp*, significantly altered the scotopic and/or photopic electroretinographic (ERG) responses of photoreceptors and bipolar cells. Cone-dominant pathways showed the most significant ERG changes. Retinal thickness, quantitated by high-resolution optical coherence tomography (OCT), and ribbon synapse morphology were not altered upon deletion of PrP^C, suggesting that the ERG changes were driven by functional rather than structural alterations.

INTRODUCTION

The normal, cellular prion protein (PrP^C) is a highly conserved, glycosylphosphatidylinositol (GPI) anchored, membrane protein expressed by many cell types, including neurons and glia of the nervous system. Expression of PrP^C is required for susceptibility to prion diseases, such as chronic wasting disease in cervids, bovine spongiform encephalopathy in cows, scrapie in sheep, and Creutzfeldt-Jakob disease (CJD) in humans. In these diseases, aberrant misfolding of PrP^C leads to the formation of PrP^{Sc}, the main component of infectious prions and central element in prion disease pathogenesis. While the role of PrP^C in disease is well understood, the normal function/s of PrP^C have been the source of debate.[1–3]

Strategies aimed at elucidating a normal function for PrP^C have typically relied on deletion of the gene encoding PrP^C, *Prnp*, in various laboratory mouse strains. While deletion of *Prnp* does not cause overt developmental, physiological, or anatomical deficiencies, investigations of prion protein knockout mice (PrPKO) have revealed multiple discreet phenotypic differences from wildtype (WT) mice, suggesting a more subtle function of PrP^C.[2,4] Among the functions proposed for PrP^C is a role in the neural synapse. Past studies have suggested that PrPKO mice have deficiencies in glutamatergic neurotransmission and altered long term potentiation and, thus, differences in behavior, learning, and memory relative to WT mice.[5–9] Unfortunately, many of these investigations used non-coisogenic PrPKO mice, which complicates the assignment of the observed phenotypes solely to deletion of the *Prnp* gene.[10–12] Evidence from studies using coisogenic PrPKO mice, such as the 129/Ola-$Prnp^{Edbg/Edbg}$ PrPKO mice[13] and the more recently created C57BL/6J-$Prnp^{ZH3/ZH3}$ PrPKO mice,[11] now provide more direct evidence for the involvement of PrP^C in neurotransmission, neuronal excitability and synaptic plasticity.[14–16] Yet, details of the role of PrP^C in the synapse remain unclear.

Here, we focused on retina to investigate a role for PrP^C in the synapse. As an extension of the CNS, retina possesses the same functional elements and neurotransmitters as brain, but because of the highly ordered anatomy of retina, the neuronal circuitry has been more clearly resolved both anatomically and by electrophysiological techniques, such as electroretinography (ERG).[17–20] In the present study, single-nuclei RNA sequencing (snRNA-seq) was used to identify the retinal cell types expressing *Prnp* mRNA transcripts, and confocal microscopy was used to study the locations of PrP^C in relation to subcellular structures involved in retinal synaptic transmission. Full-field ERG was conducted in two strains of coisogenic PrPKO mice to assess the involvement of PrP^C in retinal cell electrophysiology and/or synaptic transmission. Deficiencies

[1]Laboratory of Neurological Infections and Immunity, National Institute of Allergy and Infectious Diseases, National Institutes of Health, Hamilton, MT 59840, USA
[2]Research Technologies Branch, Rocky Mountain Laboratories, National Institute of Allergy and Infectious Diseases, National Institutes of Health, Hamilton, MT 59840, USA
[3]Department of Ophthalmology, Duke University School of Medicine, Durham, NC 27710, USA
[4]Department of Cell Biology, Duke University School of Medicine, Durham, NC 27710, USA
[5]McLaughlin Research Institute, Great Falls, MT 59405, USA
[6]Lead contact
*Correspondence: striebelj@nih.gov (J.F.S.), mikael@mclaughlinresearch.org (M.K.)
https://doi.org/10.1016/j.isci.2024.110954

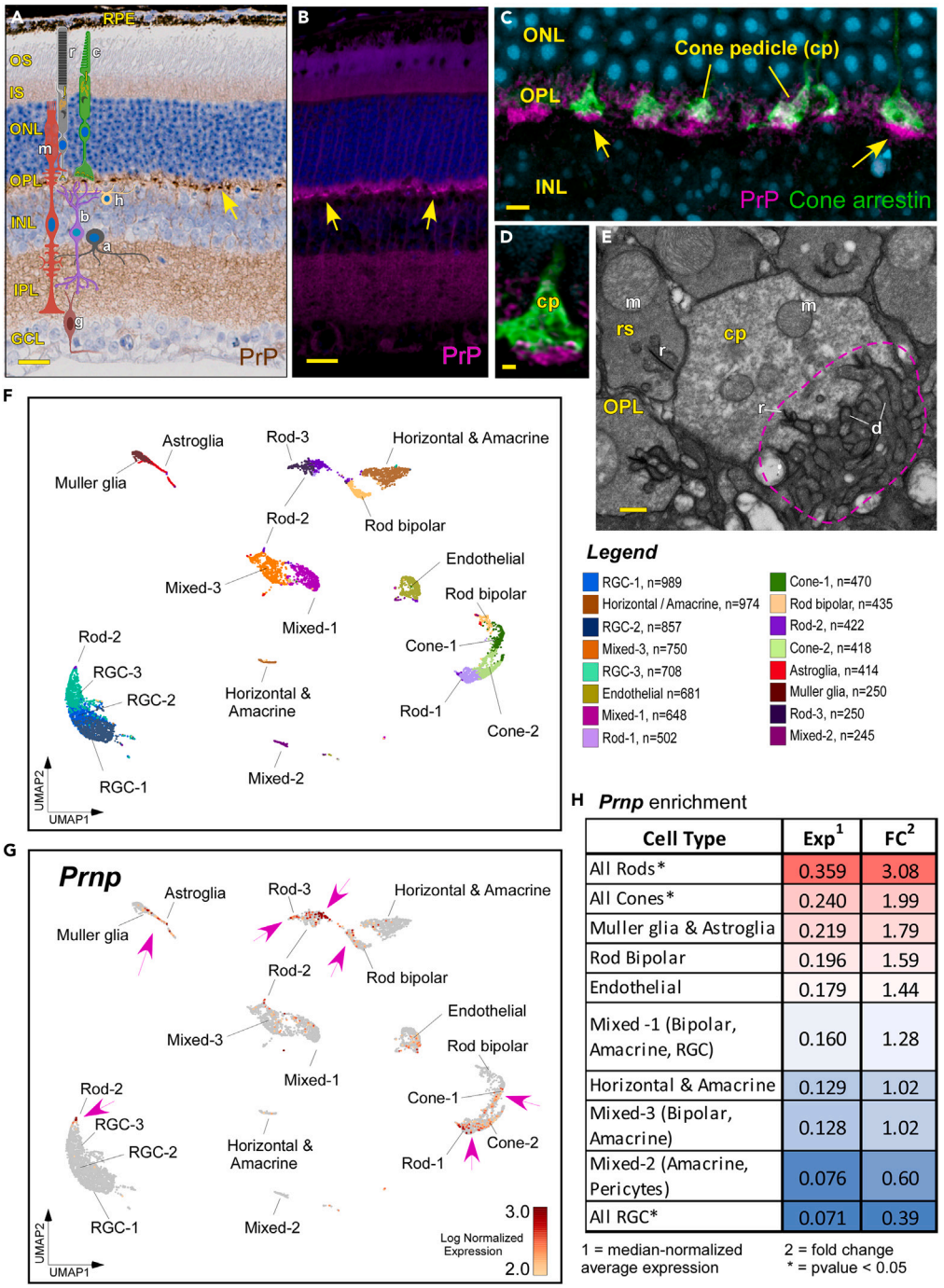

H ***Prnp*** enrichment

Cell Type	Exp[1]	FC[2]
All Rods*	0.359	3.08
All Cones*	0.240	1.99
Muller glia & Astroglia	0.219	1.79
Rod Bipolar	0.196	1.59
Endothelial	0.179	1.44
Mixed -1 (Bipolar, Amacrine, RGC)	0.160	1.28
Horizontal & Amacrine	0.129	1.02
Mixed-3 (Bipolar, Amacrine)	0.128	1.02
Mixed-2 (Amacrine, Pericytes)	0.076	0.60
All RGC*	0.071	0.39

1 = median-normalized average expression

2 = fold change
* = pvalue < 0.05

Figure 1. PrP^C expression in mouse retina, single nucleus RNA sequencing (snRNA-seq) of normal C57BL/6J mouse retina and *Prnp*-enrichment of retinal cell types

(A) In C57BL/6J mouse retina, immunohistochemical staining with anti-PrP antibody (D13) (brown) shows the darkest staining in the OPL and IPL, with faint staining in IS. PrP^C is also visible in the ONL & INL, where it appears to be on processes between cell bodies. Cartoon overlay shows cell synaptic relationships. R = rod, c = cone, m = Müller cell, h = horizontal cell, b = bipolar cell, a = amacrine cell, g = ganglion cell.

(B) The same pattern observed with immunohistochemical staining is observed in fluorescent staining with D13.

(C) A confocal maximum intensity projection (MIP) of a retinal section, triple stain shows PrP^C (magenta) concentrated at base of cone pedicles stained with cone arrestin (green), yellow arrow.

(D) A high magnification image of a cone pedicle from panel C.

Figure 1. *Continued*

(E) Electron micrograph from mouse retina, shows details of OPL, where photoreceptor synaptic terminals (rod spherules (rs) and cone pedicles (cp)) meet with dendrites (d) from bipolar, horizontal, and Müller glial cells. Magenta dotted line shows location of PrP^C. mitochondria (m), synaptic ribbons I Scale bars A, B = 25 μm, C = 2.5 μm, D = 2 μm, E = 1 μm. RPE = retinal pigmented epithelium, OS = outer segment, IS = inner segment, ONL = outer nuclear layer, OPL = outer plexiform layer, INL = inner nuclear layer, IPL = inner plexiform layer, GCL = ganglion cell layer, NFL = nerve fiber layer.

(F) 2-D UMAP projection shows 16 clusters assigned to the 9013 nuclei isolated from mouse retina. Cell types were assigned by differential expression analysis, see Figure S1. The number of nuclei per cluster are shown at right.

(G) The same cluster map as in A, shows differential analysis of *Prnp* expression among the retinal cell types. Pink arrows indicate the cell types with highest enrichment of *Prnp* mRNA.

(H) Chart shows a comparison of the median normalized expression and fold-change among the retinal cell-types identified in the nuclear isolates. Red to blue spectrum indicates high to low values, respectively. Graphic in panel A created with BioRender.com.

in specific ERG responses were found in both PrPKO mouse strains tested. These deficiencies originated in the retinal cell types and synapses where PrP^C was most highly expressed. Analysis of retinal thickness and synaptic morphology, by optical coherence tomography (OCT) and confocal microscopy, respectively, suggested that ERG differences between PrPKO and WT mice, were driven by functional rather than structural alterations.

RESULTS

PrP^C localizes to synaptic layers of retina

To understand how PrP^C might be involved in retinal synaptic function and/or structure, we first investigated the pattern of PrP^C expression in retina. Immunohistochemical and immunofluorescent staining of retinal sections showed that PrP^C was highly expressed in the synaptic layers of retina, i.e., the inner plexiform layer (IPL) and outer plexiform layer (OPL) (Figures 1A and 1B). Faint PrP^C staining observed on the outer side of the outer nuclear layer (ONL), suggested PrP^C was also present in the inner segments (IS) of the photoreceptors and light PrP^C staining was also evident on processes between the nuclei of the ONL and inner nuclear layers (INL) (Figures 1A and 1B).

The densest PrP^C appeared intermittently along the entire OPL. Co-staining with anti-cone arrestin and anti-PrP antibodies, indicated that these dense areas of PrP^C were at the base of cone synaptic terminals (pedicles) (Figures 1C and 1D) where the dendrites from horizontal, and both ON and OFF bipolar cells, synapse with cones (Figure 1E). PrP^C was also observed more diffusely in the OPL in a pattern that suggested association with the synaptic terminals (spherules) of rod photoreceptors (Figures 1A–1C).

The overall pattern of PrP^C expression (Figures 1A–1E) is consistent with the idea that PrP^C is made in the IS of photoreceptors, where the protein synthesis machinery is concentrated, transported along photoreceptor axons which traverse the ONL, and is then heavily deposited at the synaptic terminals of rod and especially, cone photoreceptors in the OPL. This pattern is supported by evidence from brain where PrP^C is known to be transported within neurons, along axons and enriched at synaptic terminals.[21] Furthermore, this same pattern is repeated for the bipolar cells where PrP^C is noted among the bipolar cell axons in the INL and heavily present in the IPL near the synapses between bipolar, amacrine and ganglion cells (Figures 1A and 1B).

Single-nuclei RNA sequencing of retina indicates *Prnp* expression is highest among photoreceptors, Müller glia and rod-bipolar cells

snRNA-seq was conducted on retinas from C57BL/6J adult mice to validate immunohistochemical staining of retina and to pinpoint the cell types expressing PrP^C. Differential expression of 23,424 gene transcripts identified within the 9013 isolated nuclei and subsequent unsupervised clustering, separated the nuclei into 16 different groups (clusters). These nuclear clusters were then assigned cell types as defined by their enrichment for key retinal cell-specific gene transcripts (Figure S1). A Uniform Manifold Approximation and Projection (UMAP), shows a 2-D representation of the defined clusters (Figure 1F).

From the nuclear isolates, we were able to identify: multiple clusters of rod and cone photoreceptors, 3 clusters of retinal ganglion cells (RGC), horizontal cells, rod bipolar cells, Müller glia, astroglia, endothelial cells and 3 clusters containing mixed cells (Figures 1F and S1). Within the mixed cell clusters, retinal pigmented epithelial (RPE), amacrine and bipolar cells were present. Microglia were not detected in the sample.

Differential analysis of *Prnp* expression among the cell clusters, suggested that photoreceptors (rods, cones), Müller glia/astrocytes and rod-bipolar cells were the cell types most enriched with *Prnp* mRNA transcripts (Figures 2G and 2H).

Localization of PrP^C with retinal synapses and synaptic-related proteins

Widefield fluorescence microscopy and confocal analysis of retinas was conducted to locate more precisely the subcellular expression of PrP^C. Because the most intense PrP^C staining was present in the OPL, we focused on localizing PrP^C relative to synaptic markers specific to this region.

In the OPL rod and cone photoreceptor neurons synapse with bipolar cells and horizontal cells. A key functional element in both rod and cone synaptic terminals is the synaptic ribbon, which functions to hold vesicles prior to their release into the synaptic cleft.[22] Triple stains for CtBP2, a marker for synaptic ribbons, PrP^C and cone arrestin indicated that PrP^C was most concentrated at the base of cone pedicles where

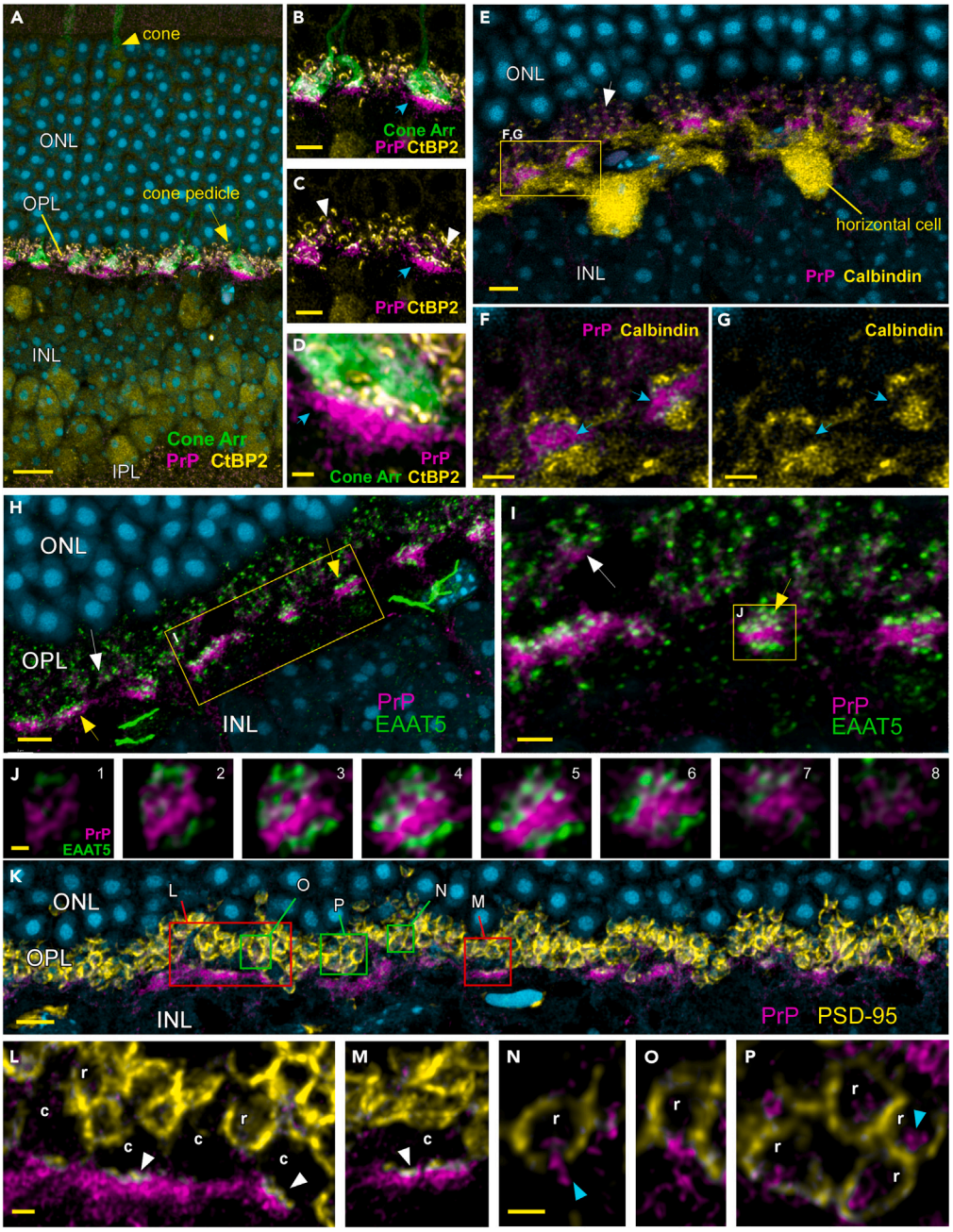

Figure 2. PrP^C localizes with photoreceptor synaptic terminals and synaptic proteins in the OPL

(A) A confocal maximum intensity projection (MIP) of a retinal section, quadruple stained shows PrP^C (magenta) concentrated at base of cone pedicles stained with Cone arrestin (green), yellow arrow.

(B–D) High magnification pictures taken from the box in A, show PrP^C staining vitread to cone pedicles (green) and the ribbon synapses marked with CTBP2 (yellow) in cone pedicles (blue arrows) and rod spherules (white arrowheads) (E) A confocal MIP shows the co-staining of horizontal cells (calbindin, yellow) and PrP^C (magenta). Tiny yellow puncta are horizontal cell dendrite tips invaginating rod spherules (white arrow), faint PrP^C (magenta) staining is adjacent to these dendrite tips.

(F and G) Dense PrP^C deposits at base of cone pedicles are surrounded by horizontal cell dendrites (blue arrows) but not directly co-localized.

(H) A triple-stained retinal section (confocal, MIP) shows the locations of PrP^C (magenta) and synaptic marker/glutamate transporter, EAAT5 (green). Note PrP^C is present near EAAT5 puncta found in both rod (white arrow) and cone (yellow arrow) synaptic terminals.

(I) High magnification view of box in H, showing PrP^C at cone and rod synaptic terminals.

(J) A series of high magnification optical sections from box in I, show a cone synaptic terminal and the relative locations of EAAT5 and PrP^C.

(K) A confocal image (MIP) shows a retinal section co-stained for PrP^C (magenta) and PSD-95 (yellow) a synaptic marker.

Figure 2. *Continued*

(L and M) High magnification, 1μm confocal sections taken from confocal image/dataset shown in K, allow inspection of the PSD-95 labeling (yellow, white arrowheads) at the base of cone (c) pedicles and its relation to the PrP^C staining (magenta).

(N–P) Also, high magnification, 1μm confocal sections taken from the confocal image/dataset shown in K, show relative positions of the PSD-95 labeling (yellow, blue arrowheads) in rod (r) spherules and its relation to the PrP^C staining (magenta). Scale bars: A = 10 μm B, C = 4μm D, E = 1 μm E = 2.0 μm F, G = 2.0 μm H, I = 5 μm J = 0.5 μm K = 2.5 μm L, N = 1.0μm.

the synaptic ribbons unite with dendrites of horizontal and bipolar cells (Figures 2A–2D). In addition, PrP^C was present adjacent to the synaptic ribbons present in rod synaptic terminals (spherules) (Figures 2B and 2C).

Co-immunostainings for PrP^C and calbindin, a marker for horizontal cells, showed that PrP^C localized very closely with horizontal cell dendrites where they invaginate both cone and rod ribbon synapses (Figure 2E). At these sites, PrP^C and calbindin did not directly colocalize (Figures 2F and 2G), suggesting the PrP^C at this location may be on bipolar cell dendrites, Müller glial processes or between dendrites.

PrP^C was also localized to synapses of the OPL using antibodies against excitatory amino acid transporter 5 (EAAT5), a synaptic protein expressed near glutamate release sites on rod spherules, cone pedicles and bipolar cells in the OPL.[23] PrP^C was directly adjacent to EAAT5 puncta present on rod spherules and cone pedicles (Figures 2H and 2I). Most strikingly, EAAT5 puncta were present on both the vitread (toward vitreous) and sclerad (toward sclera) sides of the PrP^C densities at the base of cone pedicles (Figures 2H, 2I, and 2J), indicating that PrP^C occupied the area between cone synaptic terminals and the dendrites of bipolar cell neurons.

The relationship between synaptic scaffolding protein, PSD-95 (post-synaptic density protein 95), and PrP^C (Figures 2K–2P) was also studied to understand the distribution of PrP^C in the OPL. In retina, PSD-95, has a pre-synaptic distribution on cone and rod photoreceptor synaptic terminals.[24,25] At cone synaptic terminals, small PSD-95 densities were observed just sclerad to PrP^C (Figures 2K, 2L, and 2M). Rod synaptic terminals (spherules) were heavily outlined with PSD-95 and PrP^C was observed at the breaks in PSD-95 staining where dendrites of bipolar and horizontal cells invaginate the rod synaptic terminals (Figures 2K, 2N, 2O, and 2P). Thus, co-stainings of PrP^C with synaptic markers EAAT5 and PSD-95, support previous indications that PrP^C may be involved in synaptic structure and/or function.

Retinas were also stained for Müller glial cells using an antibody against EAAT1, a glutamate uptake transporter expressed on the cell surface of astroglial cells.[23,26] Müller glia are known to influence synaptic transmission and retinal electrophysiology.[17,19] Brightest labeling of EAAT1 was detected in the synaptic layers (OPL, IPL) and among the photoreceptor cell bodies (ONL). Co-localization of PrP^C and EAAT1 in the synaptic layers (OPL, IPL) suggested Müller glia express PrP^C (Figure S2). This agrees with our snRNA-seq data (Figures 1F–1H) and with data generated by others using single cell RNA sequencing (scRNA-seq).[27]

Analysis of ERG responses in two strains of coisogenic PrPKO mice

The pattern of PrP^C staining in synaptic layers, the enrichment of *Prnp* mRNA transcripts in photoreceptors and Müller glia, and the localization of PrP^C with synaptic markers in the OPL led us to examine a potential role for PrP^C in retinal electrophysiology and synaptic function, using ERG. Because the waveforms elicited in ERG studies have been well linked to the cell types in retina,[17,19,20,28] we hypothesized that deletion of *Prnp* in mice would alter the electrical responses of the retinal cell types expressing PrP^C and/or alter the transfer of electrical response at the synapses where PrP^C was most abundant.

For ERG experiments, two PrPKO mouse strains were selected, C57BL/6J - $Prnp^{ZH3/ZH3}$ PrPKO mice and their C57BL/6J wildtype (WT) controls[11] and, the 129/Ola-$Prnp^{Edbg/Edbg}$ – PrPKO mice and their 129/Ola wildtype (WT) controls.[13] These two PrPKO strains were chosen for three reasons: **1)** both strains are coisogenic, i.e., PrPKO mice are genetically identical to their WT control, differing only in the deletion of *Prnp* gene, **2)** One strain, C57BL/6J, has pigmented eyes and the other strain, 129/Ola, does not. Lack of pigment in the RPE and choroid has been shown to alter the sensitivity of retina to synaptic/electrical testing by ERG[28–30] and thus, unpigmented 129/Ola mice offer an alternate model to uncover a phenotype in PrPKO mice. **3)** Testing of two unique PrPKO mouse strains would provide an opportunity to document potential effects of mouse background genetics, and confirmation of observed phenotypes in two PrPKO strains would further support that observed differences were due to *Prnp* deletion.

An 18-step ERG protocol (see Table S1) was conducted on WT and PrPKO mice of both strains. The protocol included assessment of scotopic (dark-adapted/rod-dominant) and photopic (light-adapted/cone-dominant) ERG responses. Mice were dark-adapted overnight and individually tested in an Espion ERG apparatus. The *amplitude* and *implicit time* of each waveform feature, and overall waveform shapes were compared to study differences in WT vs. PrPKO mice responses to light stimuli.

129/Ola PrPKO mice show deficiencies in ERG responses in dark and light-adapted conditions

In single-flash, dark-adapted tests of the 129/Ola strain, PrPKO mice had significantly reduced a-wave amplitudes at all light intensities above 0.1 cd*s/m^2 (Figure 3A; Table S2). B-wave amplitudes were also significantly reduced in PrPKO mice at the two highest light intensities (Figure 3B; Table S2). The overall waveform shapes in PrPKO and WT mice were similar, as shown in the representative responses of individual mice (Figure S3A).

Dark-adapted b-wave data was also fitted to a two-site specific binding model to isolate the rod-dominant and cone-dominant contributions to the ERG responses (Figure 3C).[31,32] Rod photoreceptors become saturated at approximately 0.1 cd*s/m^2, thus the ERG response above this intensity represents primarily a cone-driven response.[33] Significant differences were noted at 100 and 1000 cd*s/m^2, which suggested deficiencies in the cone-driven responses of PrPKO mice. To confirm this, Bmax1 and Bmax2 values which represent the rod-dominant

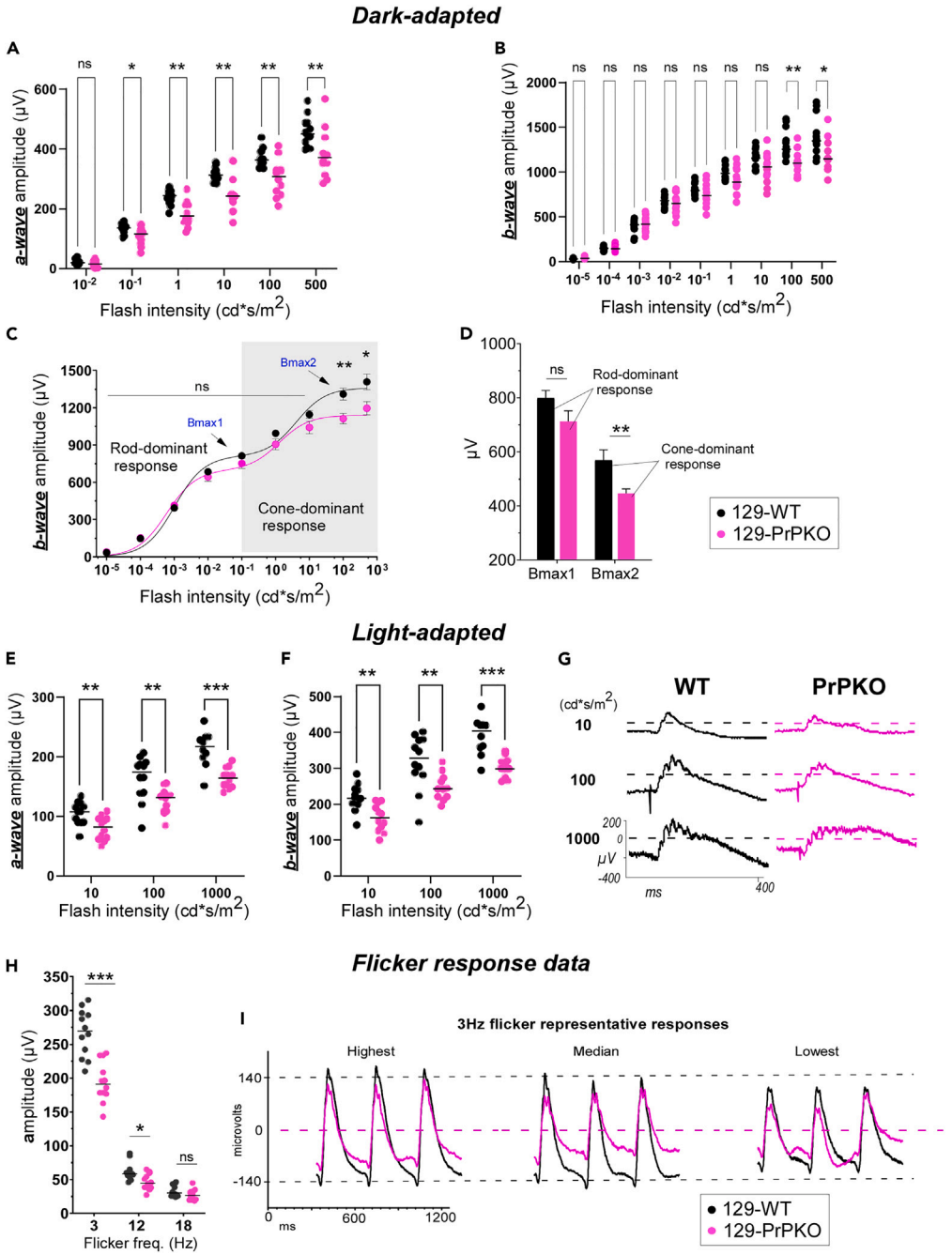

Figure 3. Comparison of ERG responses in 129/Ola WT vs. PrPKO mice

(A and B) Dark-adapted (scotopic) ERG responses (a-, b-wave amplitudes) are shown for each mouse (both eyes) at each light flash intensity.

(C) Dark-adapted b-wave data fit to a two-site specific binding model to isolate rod-driven and cone-driven contributions to ERG response (points are means +/- SEM).

(D) Bmax1 and Bmax2 mean (+/− SEM) values calculated from two-site specific binding fits of data from individual mice.

(E and F) Light-adapted (photopic) ERG responses (a-, b-wave amplitudes) are shown for each mouse at light flash intensities tested.

(G) Representative (median) ERG response waveforms for light-adapted tests.

(H) 3,12 and 18 Hz flicker light ERG responses are shown for all 129/Ola mice tested.

(I) 3Hz flicker representative waveform responses are shown for the 129/Ola mice. Waveform overlay comparisons are shown for PrPKO and WT mice with highest, median, and lowest amplitudes. Statistical analysis by Mann-Whitney test. *$p < 0.05$, **$p < 0.01$, ***$p < 0.001$, n(eyes) = 12 WT/12 PrPKO (all female, see STAR Methods for details), center lines are median.

and cone-dominant pathway responses, respectively,[31,32] were calculated for individual mice. Bmax2 values were significantly reduced in PrPKO mice indicating deficiencies in the cone-dominant pathway ERG responses (Figure 3D).

In single-flash, light-adapted experiments designed to test the cone-dominant ERG responses, the a-wave amplitudes were greatly reduced in PrPKO mice, with significant differences at all light intensities (Figure 3E; Table S2). Similarly, the b-wave amplitudes were significantly lower in PrPKO mice at all flash intensities (Figure 3F). Overall waveform shapes of PrPKO mice also appeared significantly reduced compared to WT, as shown in representative mouse responses (Figure 3G). Significant differences were also noted in the amplitudes and implicit times of the oscillatory potentials (Figures S3C and S3D; Tables S2 and S3).

In summary, the significant reductions in 129/Ola-PrPKO mice a-wave amplitudes in both light- and dark-adapted responses, suggests PrP^C is necessary for the normal photoreceptor (cone and rod) response. The differences in b-wave amplitudes in PrPKO mice reflect either a deficiency in bipolar cell response or in signal transmission at the synapses between photoreceptors and bipolar cells. The significantly decreased amplitudes and shorter implicit times in 129/Ola-PrPKO oscillatory potentials, indicate that PrP^C expression is also important to the electrical responses of inner retinal cells.

Flicker ERG responses are altered in 129/Ola PrPKO mice

In addition to the single-flash ERG tests above, responses to light flickers at three temporal frequencies (3,12 and 18 Hz) were elicited from PrPKO mice and compared to their wildtype controls. Flicker ERGs give an overview of the functionality of the main photoreceptor-bipolar cell pathways.[34] In our protocol, the 3, 12, and 18 Hz protocols were conducted to test the rod-to-rod bipolar cell pathway, the cone-to-ON-bipolar cell pathway and the cone-to-OFF-bipolar cell pathway, respectively.[34]

In 129/Ola mice, significant differences were found between PrPKO and WT mice at 3 Hz and 12 Hz in the amplitude of b-waves (Figures 3H and 3I). The highly significant differences found at 3 Hz indicate a deficiency in the rod to rod-bipolar cell pathway, which support the findings above in single-flash ERG tests, where reductions in dark-adapted a-wave and b-wave responses were observed. Likewise, the significant difference at 12 Hz points to a deficiency in the cone-to-ON bipolar cell pathway, where the highest density of PrP^C was located.

C57BL/6J PrPKO mice show deficiencies in dark-adapted ERG responses

In the C57BL/6J mouse strain, deletion of PrP^C had a similar affect in dark-adapted ERG responses (Figure 4). A-wave amplitudes were significantly reduced in PrPKO mice at all light flash intensities above 0.1 cd*s/m^2, and b-waves were significantly different at 2 of 9 light intensities (Figures 4A and 4B; Table S2). A two-site specific binding model fit of the b-wave data indicated significant differences at 0.01 and 0.1 cd*s/m^2. Calculation of Bmax1 and Bmax2 values showed significant reductions in the Bmax1 values of PrPKO mice (Figures 4C and 4D), suggesting deficiencies in the rod-dominant responses. Interestingly, these differences occurred at the flash intensities where rod photoreceptors are becoming saturated, and a transition to a cone-dominant response is occurring.

Light-adapted tests of cone-driven responses, however, were not significantly different in C57BL/6J WT vs. PrPKO mice (Figures 4E, 4F, and 4G). This lack of effect in the light-adapted tests, may be a result of the presence of pigment in C57BL/6J mice. Pigment in retina reduces light scatter and thus, the overall sensitivity of the retina.[35]

Representative waveforms of C57BL/6J WT and PrPKO mice are shown in supplemental figures and though reduced, they were not significantly different in their overall shapes (Figures S4A and S4B). Amplitudes and implicit times of oscillatory potentials were also not significantly different in comparisons of C57-WT and -PrPKO mice (Figures S4C and S4D; Tables S2 and S3).

Furthermore, the altered flicker ERG responses observed in 129/Ola-PrPKO mice were not corroborated in PrPKO mice on the C57BL/6J strain (Figure 4H). The lack of pigment in 129/Ola retina may also influence the amplitude of responses to rapid light flashes and could explain these ERG differences found between the 129/Ola and C57BL/6J strains.

Gross retinal morphology is not affected by deletion of *Prnp*

To understand potential reasons for changes in ERG responses in PrPKO mice, retinas from WT and PrPKO mice of C57BL/6J and 129/Ola strains were compared for differences in gross retinal structure using immunohistochemical staining, OCT and fundus imaging of retina.

The retinas of 129/Ola-PrPKO and -WT mice appeared healthy and nearly identical by hematoxylin and eosin (H&E) staining, as did the C57BL/6J-PrPKO and -WT retinas (Figure 5A). Black pigment (melanosomes) was present in the retinal pigmented epithelium and choroid layers of the C57BL/6J retinas, but not in the 129/Ola retinas (Figure 5A). PrP^C was found in WT mice in the OPL, IPL, IS and ONL as seen in Figure 1 (Figure 5B). As expected, in both strains of PrPKO mice there was no PrP^C staining in retina (Figure 5B).

Retinal fundus images taken from both eyes of all experimental mice, showed normal retinal vasculature in WT and PrPKO mice from both strains (Figure 5C). Again, pigment was obvious in the images from C57BL/6J PrPKO and WT mice, but not in 129/Ola mice (Figure 5C).

A detailed analysis of OCT images from all mice (129/Ola and C57BL/6J) used in the ERG study (Figures 5D and 6A–6D) was also conducted to determine if differences in retinal thickness correlated with ERG changes observed in PrPKO mice. In 129/Ola WT vs. PrPKO mice, quantitation of layer thickness from OCT cross-sections taken at superior, central and inferior points did not show significant differences in whole retinal thickness or in individual retinal layers (Figures 6A and 6B). In the C57BL/6J strain, significant differences were also not observed in whole retinal thickness, though significant differences were noted in some retinal layers in PrPKO mice on the C57BL/6J strain (Figures 6C and 6D). Overall, PrP^C deletion was not associated with changes in gross retinal structure and ERG differences could not be explained by gross anatomical differences between WT and PrPKO retinas.

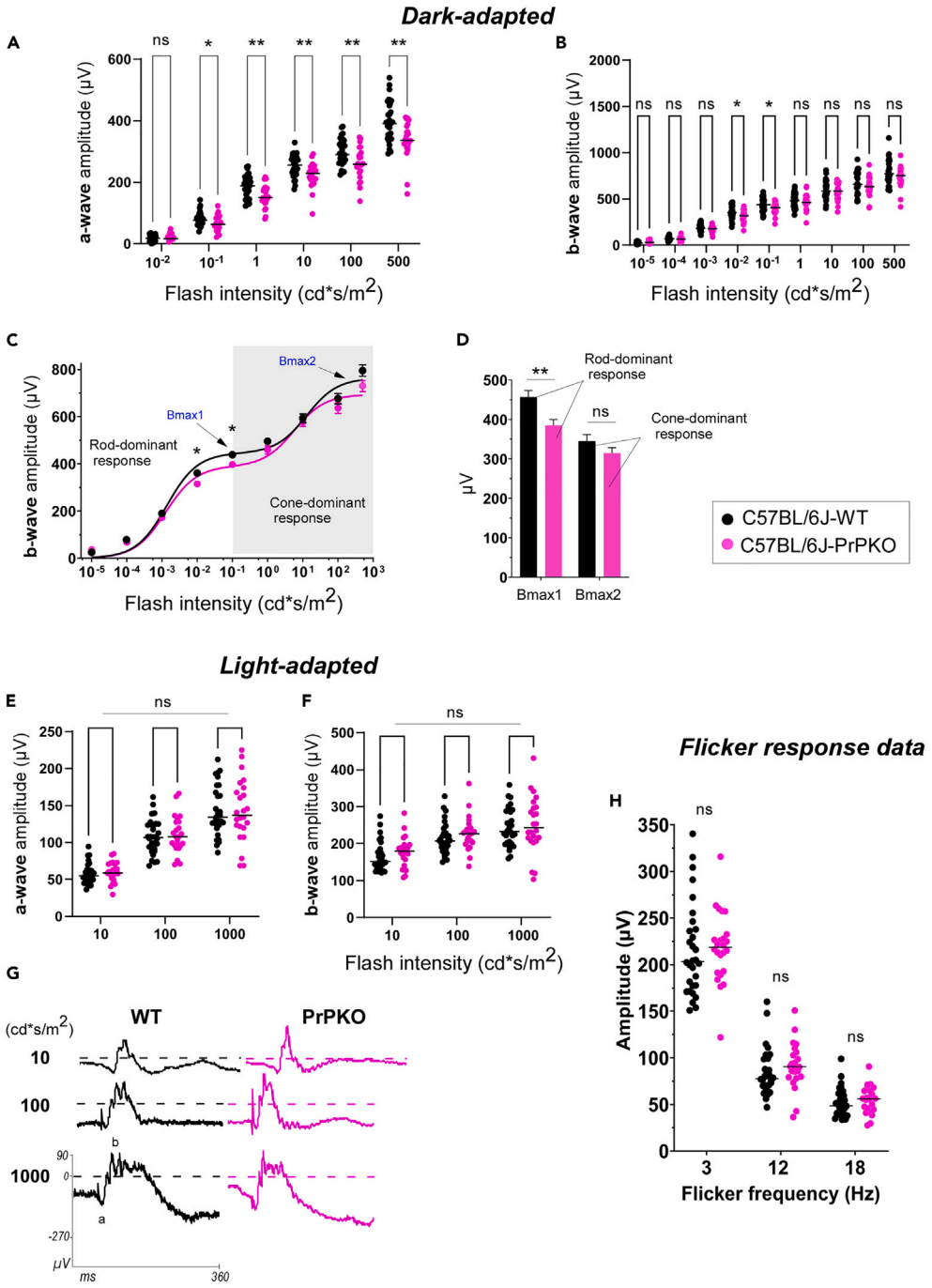

Figure 4. Comparison of ERG responses in C57BL/6J WT vs. PrPKO mice

(A and B) Dark-adapted (scotopic) ERG responses (a-, b-wave amplitudes) are shown for each mouse (both eyes) at each light intensity.

(C) Dark-adapted b-wave data fit to a two-site specific binding model to isolate rod-driven and cone-driven contributions to ERG response (points are mean +/- SEM).

(D) Bmax1 and Bmax2 mean (+/− SEM) values calculated from two-site specific binding fits of data from individual mice.

(E and F) Light-adapted (photopic) ERG responses (a-, b-wave amplitudes) are shown for each mouse (both eyes) at light flash intensities tested.

(G) Representative (median) ERG response waveforms for light-adapted tests.

(H) 3,12 and 18 Hz flicker light ERG responses are shown for all C57BL/6J mice tested. Statistical analysis by Mann-Whitney test. *$p < 0.05$, **$p < 0.01$, ***$p < 0.001$, n (eyes) = 30 WT/24 PrPKO (males and females combined, no significant difference between genders was observed), center lines are median.

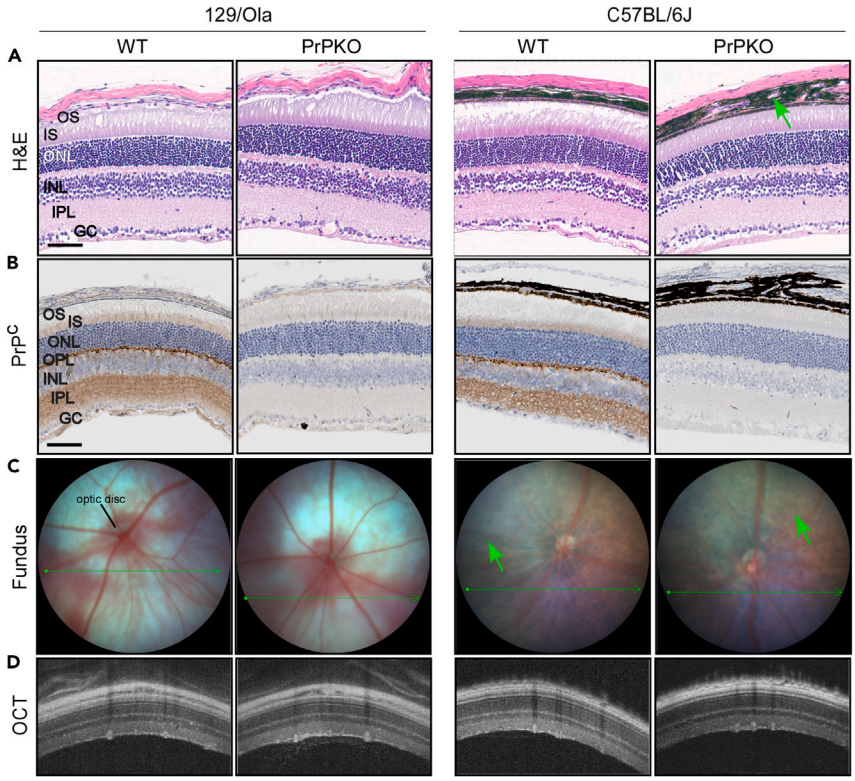

Figure 5. Comparison of overall retinal structure in two strains of PrPKO and WT mice

(A) Hematoxylin and eosin (H&E) staining of retinal sections from PrPKO and WT mice are similar, in both mouse strains. Pigment in the choroid and RPE is present in C57BL/6J strain (green arrows), but not in 129/Ola strain.

(B) Immunohistochemical staining with anti-PrP antibody, D13, shows heaviest PrP^C in the synaptic layers (OPL, IPL) and less PrP^C in the IS, ONL and INL. Patterns of staining are very similar between mouse strains. PrP^C is not expressed by PrPKO mice.

(C) Fundus images taken in live mice are compared between WT and PrPKO mice of both strains. These images show similar vasculature, and lack of retinal anomalies which could indicate retinal genetic disease. In C57BL/6J mice, pigment at back of retina appears as dark shadows (large green arrows), pigment is not present in 129/Ola mice. Long thin green arrows indicate where cross-sectional optical coherence tomography (OCT) pictures were taken for panels in D (D) OCT sections images show layers of retina in live mice. Long, thin, dark vertical lines are shadows cast by blood vessels. Scale bars in A = 50μm and applies to panels A, B.

Deletion of *Prnp* does not alter architecture of photoreceptor ribbon synapses

The modified ERG responses of the photoreceptors and bipolar cells in both C57BL/6J and 129/Ola PrPKO mice could be explained by alterations in ribbon synapse morphology. To assess OPL synaptic architecture, retinas were triple stained for CtBP2, a synaptic ribbon marker,[22] Pikachurin, a synaptic cleft marker,[36] and PKCα, a protein found in rod bipolar cells and their dendrites,[37,38] which invaginate ribbon synapses. Synaptic ribbon morphology, the placement of Pikachurin within the synaptic cleft, and the postsynaptic rod bipolar cell dendrite terminals appeared nearly identical in confocal images comparing WT and PrPKO of both C57BL/6J and 129/Ola mouse strains, (Figures 7A–7D). Quantitative assessment of ribbon synapse features also showed no significant differences (Figures 7E and 7F).

Additionally, because the most significant deficiencies in ERG responses were observed in cone-dominant pathways in 129/Ola-PrPKO mice, we examined the synaptic architecture of cone pedicles and cone-to-ON bipolar synapses. Significant differences were not found in cone pedicle volume, cone density or the number of synaptic ribbons per cone (Figures 7G–7J). Thus, ERG response differences in cone-dominant pathways in 129/Ola-PrPKO mice could not be linked to anatomical changes in ribbon synapse morphology or cone pedicles.

DISCUSSION

A role for PrP^C in mouse retinal synapses was initially investigated by determining where PrP^C and *Prnp* mRNA transcripts were localized. *Prnp* mRNA transcripts were detected by snRNA-seq primarily in photoreceptors (rods, cones), Müller glia and rod bipolar cells. Co-staining of PrP^C with synaptic markers EAAT5, PSD-95, and CtBP2, showed PrP^C was highly expressed adjacent to ribbon synapses at rod and cone synaptic terminals in the OPL. Confocal microscopy suggested that the PrP^C localized to synapsing dendrites of bipolar and horizontal cells. Here and in our previous study, PrP^C was not directly localized to horizontal cells, but did show some colocalization with secretagogin, a marker of some cone bipolar cell subtypes.[38] Thus, PrP^C at these postsynaptic locations was most likely on dendrites of bipolar cells or the processes of

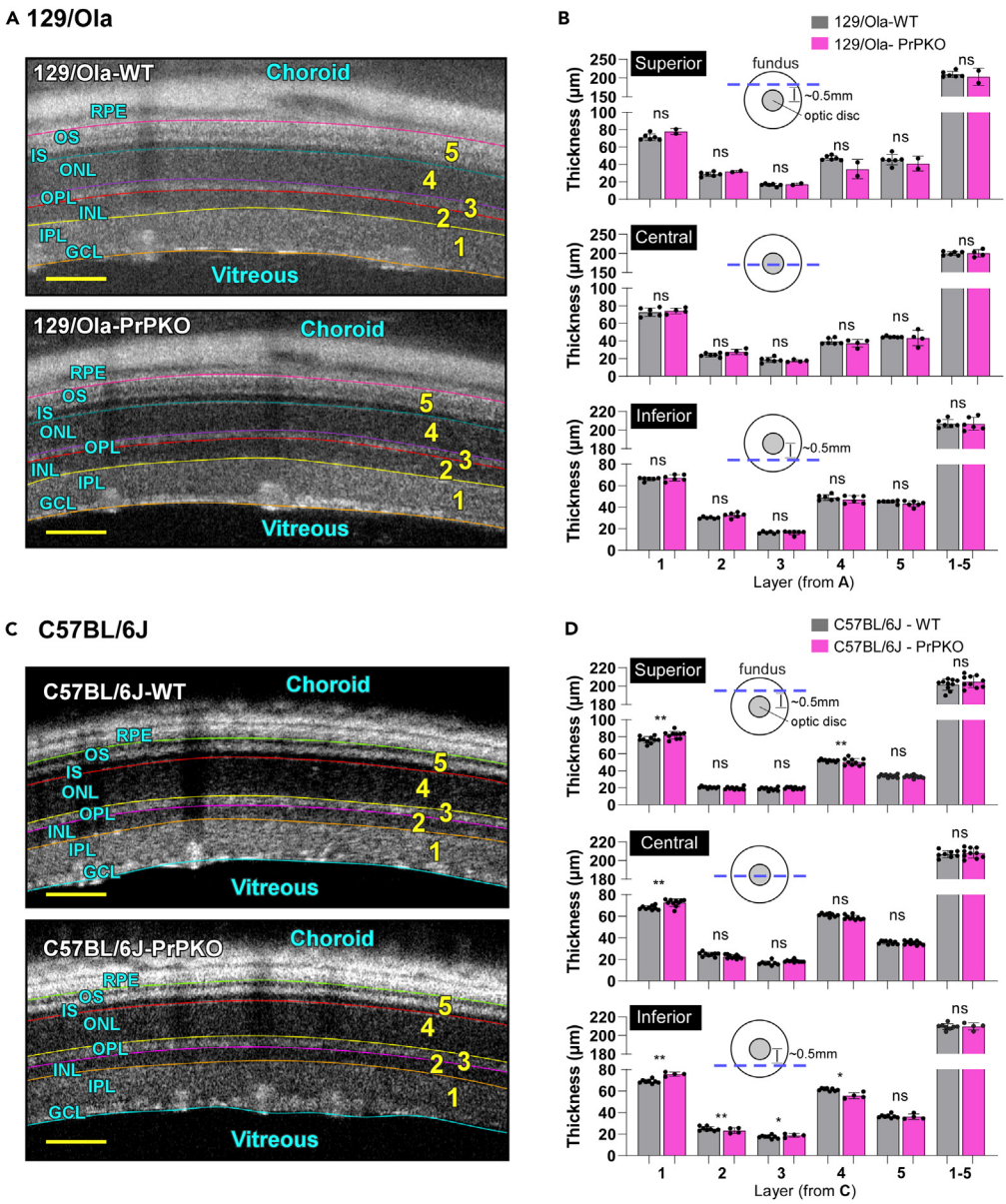

Figure 6. Analysis of retinal thickness by optical coherence tomography (OCT)

(A) Example OCT sections from 129/Ola WT and PrPKO mice with layers 1–5 marked with colored lines for thickness analysis.

(B) Layer thickness analysis for superior, central, and inferior OCT sections from 129/Ola mice.

(C) Example OCT sections from C57BL/6J WT and PrPKO mice with layers 1–5 marked with colored lines for thickness analysis.

(D) Layer thickness analysis for superior, central and inferior OCT sections from C57BL/6J mice. RPE = retinal pigmented epithelium, OS = outer segment, IS = inner segment, ONL = outer nuclear layer, OPL = outer plexiform layer, INL = inner nuclear layer, IPL = inner plexiform layer, GC = ganglion cell layer. Statistical analysis by Mann-Whitney test. *$p < 0.05$, **$p < 0.01$, ***$p < 0.001$, each point on graphs represents 1 retina, bars represent mean values, +/−SD. Scale bars in A, C = 100 µm.

Müller glia which are also present among these synapses. It is also possible that PrPC was expressed on the cell surface or in the extracellular matrix, between the dendrites, acting as a structural protein stabilizing synapses. These data led us to hypothesize that deletion of *Prnp* would alter the electrophysiological responses of retina, affecting the cells and synapses where PrP^C and/or *Prnp* mRNA transcripts were most highly expressed.

ERG experiments confirmed this hypothesis. When *Prnp* was deleted, portions of the rod and cone photoreceptor-driven pathways had significantly reduced responses to light stimuli. The most widespread effect of *Prnp* deletion was observed in significant deficits in the dark-adapted a-wave amplitudes in both C57BL/6J and 129/Ola PrPKO mice. The a-wave portion of the dark-adapted ERG response originates in

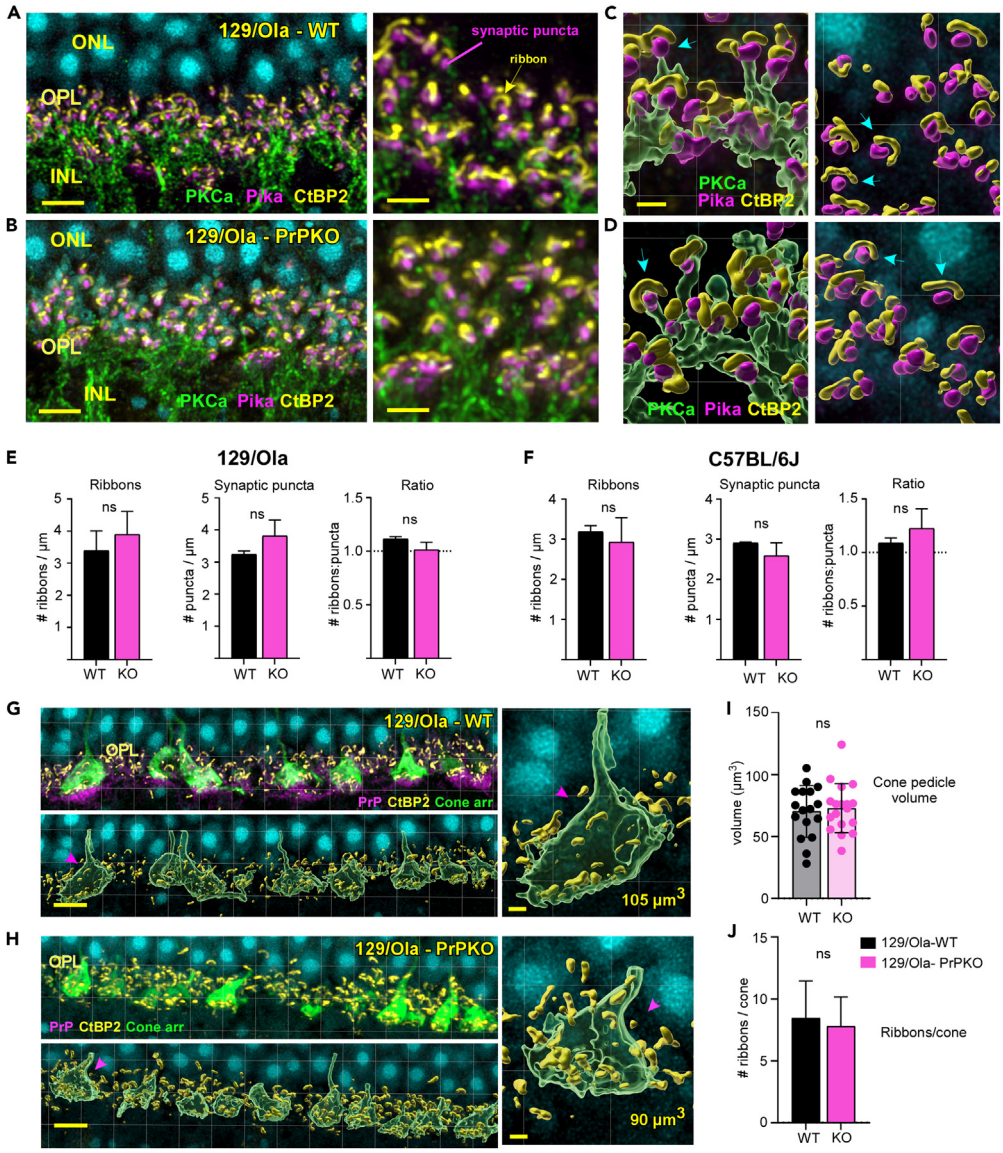

Figure 7. Morphometric analysis of ribbon synapses and cone pedicle anatomy

(A and B) Confocal maximum intensity projections show representative retinal sections from 129/Ola WT and PrPKO mice. PKCα (green) marks cell bodies and dendrites of rod bipolar cells, CtBP2 (yellow) marks synaptic ribbons and Pikachurin (magenta) is a protein present in the cleft of ribbon synapses.

(C and D) 3D surfaces were rendered using IMARIS software 9.9.1. to enable quantitation of ribbons and synaptic puncta, assessment of 3D morphology, and relative associations of synaptic ribbons, Pikachurin and rod-bipolar cell dendrites.

(E and F) Quantitation of ribbons (CtBP2), synaptic cleft puncta (Pikachurin) and ratio of ribbons to synaptic puncta are shown in graphs for both 129/Ola and C57BL/6J retinas.

(G and H) Cone pedicle (green) and ribbon synapse (yellow) 3D surfaces were rendered using IMARIS software 9.9.1. For 129/Ola -WT and PrPKO, top panels show pre-rendered confocal image and bottom panels show 3D rendered images. Example cone pedicles with volume calculation are shown at right. Each cone pedicle was rotated in 3D to study associations with ribbon synapses (yellow).

(I and J) Quantitative data from analysis of confocal datasets in E, are shown for cone pedicle volumes, and the number of ribbon synapses per cone pedicle. Scale bars: A, B = 4 µm (left), 2 µm (right) C, D = 1 µm G, H = 5 µm (left), 1 µm (right). Statistical analysis by Mann-Whitney test. *$p < 0.05$, **$p < 0.01$, ***$p < 0.001$, bars represent mean values, +/− SD.

rod photoreceptors, the cells that possess the highest *Prnp* transcript enrichment. In mouse retina, 97% of the photoreceptors are rods and the remaining 3% are cones.[39] Thus, it follows that rods would exhibit a significant change in ERG in response to *Prnp* deletion. Furthermore, the reduction in 3Hz flicker responses in 129/Ola-PrPKO mice reflects a deficiency in the rod-to-rod bipolar cell signal transfer, supporting the necessity for PrP^C expression at the rod-to-rod bipolar cell synapses in the OPL.

Interestingly, in the 129/Ola PrPKO mice, the light-adapted a-wave and b-wave amplitudes showed significant reduction at all flash intensities. Light-adapted ERG responses reflect the cone-dominant response to light stimuli. The reduction in a-waves supports that there is a deficiency in cones themselves. In contrast, the reduced b-waves can be attributed to bipolar cell/Müller glia deficiencies or, a defect in the synapses between cones and bipolar cells. Additionally, it is possible that the reduced cone response is sustained across the synapse, resulting in a similarly reduced bipolar cell response, and subsequent reduction in b-wave amplitude.

Moreover, the significant differences in b-wave amplitudes found in dark-adapted tests of 129/Ola mice (and partially in C57BL/6J), provide additional evidence that cone-driven pathways are most significantly affected by PrP^C deletion. In dark-adapted tests, rod photoreceptors become saturated at flash intensities greater than 0.1 cd*s/m^2, therefore dark-adapted ERG tests at these higher intensities reflect cone-driven responses. These cone-dominant pathway results offer strong evidence that PrP^C is involved in synaptic transmission, as PrP^C density is highest at the base of cone pedicles where hundreds of specialized cell-to-cell synapses exist.

While the dark-adapted (rod-pathway) responses were significantly reduced in PrPKO mice of both C57BL/6J and 129/Ola strains, the light-adapted (cone-pathway) response was abnormal only in the 129/Ola PrPKO mice. The lack of pigment in the 129/Ola mice may explain this difference, as lack of pigment can lead to differences in ERG, often increasing the sensitivity of retina to light stimuli.[29,35] Another possibility is that a modifier gene differing between the two strains might be responsible for synaptic scaling in the C57BL/6J PrPKO mice, thereby attenuating the deficit seen under light-adapted (cone-pathway) conditions in the 129/Ola PrPKO mice. A similar situation has been reported previously in a model of retinal dysfunction.[40,41] Here, the use of PrPKO mice on two mouse backgrounds (129/Ola and C57BL/6J) was advantageous in elucidating these effects of *Prnp* deletion on retinal electrophysiology.

A previous study by Frigg and colleagues, reported that ERG tests of PrPKO mice were unremarkable, but data was not shown.[42] Because of the lack of details, it is difficult to parse out the potential reasons for the differences found in our work versus Frigg et al. One possible explanation lies in the PrPKO mice used. Frigg et al. used two PrPKO mouse strains, one on a BALB/c background and one on a C57BL/6 background, the strain of PrPKO mice used in ERG recordings was not specified. Importantly, both PrPKO strains, in their study, were generated by backcrossing PrPKO mice of different origins to new WT strains. While backcrossing is effective at switching most previous mouse background genes to a new mouse background, it does not remove genes flanking the knockout locus.[10] Mouse background genes have been shown to significantly affect ERG responses.[35]

Other vision related phenotypes have been observed upon deletion of *Prnp*. A 2005 study, by Criado et al. found that PrPKO mice differed dramatically from WT mice in their ability to use visuospatial cues.[16] This defect could be explained by the altered ERG responses noted here in PrPKO mice, or alternatively, attributed to a deficiency in visual processing in the optic tract, lateral geniculate bodies and/or the visual cortex. Ashok et al. have also investigated a role for PrP^C in eye, finding that PrPKO mice (on a mixed 129xC57BL/6J background), have increased ocular pressure and alterations in extracellular matrix (ECM) protein structure.[43] Increased ocular pressure, as observed in glaucoma, can affect ERG response by altering the amplitude of photopic negative response (PhNR), a measurement of retinal ganglion cell health.[44] Our ERG studies did not find differences in PhNR amplitude measurements between PrPKO and WT mice (Table S2). However, the observed alterations in ECM protein structure in these PrPKO mice could influence retinal synaptic transmission.[45]

One explanation for how PrP^C might influence synaptic transmission involves the hypothesis that PrP^C is a cell surface scaffolding protein or adhesion molecule. GPI-anchored proteins are known to act as scaffolding proteins and/or adhesion molecules in the ECM.[45,46] PrP^C may act to bring two or more proteins into a stable configuration, allowing for more efficient signal transduction. There is evidence from others to support this role for PrP^C.[47–50] From our study, the localization of PrP^C at the synapse and the ERG data support PrP^C acting to enhance synaptic transmission. Because ERG responses were significantly affected, but not abolished upon deletion of *Prnp*, a discreet role as a scaffolding protein or adhesion molecule seems rational.

Synaptic adhesion molecules, such as Lrit1, Lrit3, Elfn1, Elfn2, Lrfn2 and Nyctalopin, have been shown to act at synapses in the OPL, modulating ERG responses.[41,51–56] Studies of *Lrit1*-null mice support the idea that PrP^C could be acting as a synaptic adhesion molecule.[41,56] *Lrit1* is a recently identified, retinal adhesion molecule and like PrP^C is found at photoreceptor synaptic termini, mainly in cone pedicles. When ERG recordings were compared between *Lrit1*-null mice and WT mice, significant differences were found in light-adapted b-waves, indicating impairment of synaptic transmission at cone-to-bipolar cell synapses.[41,56] While this is a similar, but not the exact ERG phenotype we observed in PrPKO mice, it indicates how adhesion molecules might modulate ERG responses.

Because differences in gross retinal anatomy or ribbon synapse morphology, assessed by confocal microscopy, did not correlate with ERG deficiencies in both PrPKO mouse strains, functional involvement of PrP^C at the synapse, rather than structural, is more likely. It may be that PrP^C works collectively with one or more proteins to enhance or attenuate synaptic transmission. There are multiple GPI-anchored neural/synaptic proteins, like PrP^C, that function to mediate protein-to-protein interactions or act as co-receptors.[57] Elucidating the precise function of PrP^C, may require study of mouse models where PrP^C and one or more additional proteins of suspected, related function are knocked out. Alternatively, knockdown of PrP^C in specific cells, using adeno-associated virus-mediated delivery of shRNA, could be done to target rods, cones, rod bipolar cells, cone-ON bipolar cells, cone-OFF bipolar cells, and Müller glia. This could facilitate clarification of the role of PrP^C by limiting unknown compensatory mechanisms which conceal its function under normal circumstances, or it may exaggerate the deletion-related phenotype, making it more apparent.

Finally, new efforts to treat human prion diseases, such as CJD and Fatal Familial Insomnia, rely on knockdown of PrP^C expression in neural tissues using anti-sense oligonucleotides.[58–61] The consequences of PrP^C knockdown in humans are unknown. Thus, clarifying the function of PrP^C is of high importance.

Limitations of the study

In our study of PrP^C in retina, snRNA-seq was used instead of scRNA-seq to locate the cell types expressing *Prnp* transcripts. SnRNA-seq was chosen because of its advantages in analyzing complex, hard-to-dissociate tissues like brain and retina. While comparisons between the two techniques have provided similar results,[62,63] snRNA-seq may have affected our identification of the retinal cell types expressing *Prnp*. ScRNA-seq analyzes transcripts in both nucleus and cytoplasm and could provide a more in-depth assessment of *Prnp* expression.

Additionally, in our study of PrP^C localization in retina, despite repeated attempts, we were not able to label PrP^C with immunogold for electron microscopy (EM) analysis. Historically, PrP^C has been very difficult to immunolabel in preparation for EM.[64,65] This has limited our and others' ability to localize PrP^C at the ultrastructural level.

Lastly, our data do not definitively exclude a structural role for PrP^C in synaptic function, i.e., the possibility still exists that deletion of PrP^C could alter some feature of synaptic morphology, not detected in our studies, and explain the ERG alterations found in PrPKO mice. Our comparative analysis of ribbon synapse architecture in WT and PrPKO mice relied on confocal microscopy, with qualitative assessment of pre- and postsynaptic structure as well as quantitative assessment of presynaptic parameters. However, future studies comparing WT and PrPKO ribbon synapses might benefit from a focused study of pre-and post-synaptic structures using transmission electron microscopy and/or focused ion beam-scanning electron microscopy.

RESOURCE AVAILABILITY

Lead contact

Further information and requests for resources and reagents should be directed to and will be fulfilled by the lead contact, J.S. (striebelj@niaid.nih.gov).

Materials availability

All reagents used in this study are available from scientific supply companies, except the anti- PrP^C antibody D13, which depending on supply, is available upon request. Prnp-null mice (ZH3PrPKO and 129/Ola-PrPKO) used in the experiments are available upon request and wildtype control mice are available from Jackson Laboratories (Bar Harbor, ME, USA).

Data and code availability

- RNA-seq data have been deposited to GEO and are publicly available. Accession number is also listed in the key resources table. GEO accession: GSE264257 https://www.ncbi.nlm.nih.gov/geo/query/acc.cgi?acc=GSE264257. Our analysis of the differentially expressed genes between cell types are reported in the supplemental tables.
- This paper does not report original code.
- Any additional information required to reanalyze the data reported in this paper is available from the lead contact upon request.

ACKNOWLEDGMENTS

The authors thank Dan Long, Tina Thomas, and Lori Lubke for technical histology assistance, Jeffrey Severson (RML), Tara Weisz (Duke Univ.) for animal husbandry, and Drs. Suzette Priola, Clayton W. Winkler, Simote T. Foliaki for advice on manuscript preparation. C57BL/6J – *Prnp*$^{ZH3/ZH3}$ PrPKO mice provided by A. Aguzzi (University of Zurich, Zurich, Switzerland) via Mark Zabel (Colorado State University, Fort Collins, CO, USA) and *Prnp*$^{Edbg/Edbg}$ – PrPKO mice on 129/Ola background and co-isogenic WT 129/Ola mice were both kindly provided by Jean Manson (University of Edinburgh, Edinburgh, Scotland, UK). For work on snRNASeq datasets, we kindly thank Dan Sturdevant of the Genomics Research Section, Research Technologies Branch, Rocky Mountain Laboratories, NIAID, NIH; Hamilton, MT., USA. The graphical abstract and Figure 1 contain objects created with BioRender.com.

This research was supported by the Intramural Research Program (DIR) of the National Institute of Allergy and Infectious Diseases (NIAID) of the United States, National Institutes of Health (NIH); by extramural funding to M.K. from the National Eye Institute (NEI; R21EY033057) and the National Institute of General Medical Sciences (NIGMS; P20GM152335). This research was also supported by extramural funding to C.B.R. from NEI (NIH RO1EY031748), NEI (P30EY05722 – Duke Vision Research Core Grant) and FFB-Free Family AMD award.

AUTHOR CONTRIBUTIONS

J.S. designed study, gathered and analyzed data from all sources, and wrote the manuscript. M.K. designed the study, gathered and analyzed data from ERG and OCT, and assisted in writing the manuscript. J.C. gathered and analyzed data from snRNA-seq experiments and edited the manuscript. B.R. assisted in designing the study and edited the manuscript. J.L. gathered and analyzed confocal datasets and edited the manuscript. C.S. prepared samples for electron microscopy, gathered and analyzed electron microscopy data, and edited the manuscript. B.C. assisted in study design and assisted in preparing manuscript. C.B.R. assisted in study design and edited the manuscript. E.D.R. analyzed OCT data.

DECLARATION OF INTERESTS

The authors declare no competing interests.

STAR★METHODS

Detailed methods are provided in the online version of this paper and include the following:

- Retinal nuclei isolation for single nucleus RNA sequencing
- Single nuclei RNA library construction and next-generation sequencing
- Confocal microscopy
- Confocal image processing and analysis
- Electron microscopy sample preparation
- Transmission electron microscopy
- Optical coherence tomography (OCT), fundus imaging and assessment for retinal degeneration genes
- *In vivo* retinal function analysis by electroretinography (ERG)

● QUANTIFICATION AND STATISTICAL ANALYSIS

SUPPLEMENTAL INFORMATION

Supplemental information can be found online at https://doi.org/10.1016/j.isci.2024.110954.

Received: May 2, 2024
Revised: July 15, 2024
Accepted: September 10, 2024
Published: September 13, 2024

REFERENCES

1. Peggion, C., Bertoli, A., and Sorgato, M.C. (2017). Almost a century of prion protein(s): From pathology to physiology, and back to pathology. Biochem. Biophys. Res. Commun. *483*, 1148–1155. https://doi.org/10.1016/j.bbrc.2016.07.118.
2. Watts, J.C., Bourkas, M.E.C., and Arshad, H. (2018). The function of the cellular prion protein in health and disease. Acta Neuropathol. *135*, 159–178. https://doi.org/10.1007/s00401-017-1790-y.
3. Wulf, M.A., Senatore, A., and Aguzzi, A. (2017). The biological function of the cellular prion protein: an update. BMC Biol. *15*, 34. https://doi.org/10.1186/s12915-017-0375-5.
4. Castle, A.R., and Gill, A.C. (2017). Physiological Functions of the Cellular Prion Protein. Front. Mol. Biosci. *4*, 19. https://doi.org/10.3389/fmolb.2017.00019.
5. Collinge, J., Whittington, M.A., Sidle, K.C., Smith, C.J., Palmer, M.S., Clarke, A.R., and Jefferys, J.G. (1994). Prion protein is necessary for normal synaptic function. Nature *370*, 295–297. https://doi.org/10.1038/370295a0.
6. Pathmajeyan, M.S., Patel, S.A., Carroll, J.A., Seib, T., Striebel, J.F., Bridges, R.J., and Chesebro, B. (2011). Increased excitatory amino acid transport into murine prion protein knockout astrocytes cultured in vitro. Glia *59*, 1684–1694. https://doi.org/10.1002/glia.21215.
7. Khosravani, H., Zhang, Y., Tsutsui, S., Hameed, S., Altier, C., Hamid, J., Chen, L., Villemaire, M., Ali, Z., Jirik, F.R., and Zamponi, G.W. (2008). Prion protein attenuates excitotoxicity by inhibiting NMDA receptors. J. Gen. Physiol. *131*, i5. https://doi.org/10.1085/JGP1316OIA5.
8. Schmitz, M., Greis, C., Ottis, P., Silva, C.J., Schulz-Schaeffer, W.J., Wrede, A., Koppe, K., Onisko, B., Requena, J.R., Govindarajan, N., et al. (2014). Loss of prion protein leads to age-dependent behavioral abnormalities and changes in cytoskeletal protein expression. Mol. Neurobiol. *50*, 923–936. https://doi.org/10.1007/s12035-014-8655-3.
9. Ferreira, D.G., Temido-Ferreira, M., Vicente Miranda, H., Batalha, V.L., Coelho, J.E., Szegö, É.M., Marques-Morgado, I., Vaz, S.H., Rhee, J.S., Schmitz, M., et al. (2017). alpha-synuclein interacts with PrP(C) to induce cognitive impairment through mGluR5 and NMDAR2B. Nat. Neurosci. *20*, 1569–1579. https://doi.org/10.1038/nn.4648.
10. Striebel, J.F., Race, B., and Chesebro, B. (2013). Prion protein and susceptibility to kainate-induced seizures: genetic pitfalls in the use of PrP knockout mice. Prion *7*, 280–285. https://doi.org/10.4161/pri.25738.
11. Nuvolone, M., Hermann, M., Sorce, S., Russo, G., Tiberi, C., Schwarz, P., Minikel, E., Sanoudou, D., Pelczar, P., and Aguzzi, A. (2016). Strictly co-isogenic C57BL/6J-Prnp-/- mice: A rigorous resource for prion science. J. Exp. Med. *213*, 313–327. https://doi.org/10.1084/jem.20151610.
12. Herms, J., Tings, T., Gall, S., Madlung, A., Giese, A., Siebert, H., Schürmann, P., Windl, O., Brose, N., and Kretzschmar, H. (1999). Evidence of presynaptic location and function of the prion protein. J. Neurosci. *19*, 8866–8875. https://doi.org/10.1523/JNEUROSCI.19-20-08866.1999.
13. Manson, J.C., Clarke, A.R., Hooper, M.L., Aitchison, L., McConnell, I., and Hope, J. (1994). 129/Ola mice carrying a null mutation in PrP that abolishes mRNA production are developmentally normal. Mol. Neurobiol. *8*, 121–127. https://doi.org/10.1007/BF02780662.
14. Matamoros-Angles, A., Hervera, A., Soriano, J., Martí, E., Carulla, P., Llorens, F., Nuvolone, M., Aguzzi, A., Ferrer, I., Gruart, A., et al. (2022). Analysis of co-isogenic prion protein deficient mice reveals behavioral deficits, learning impairment, and enhanced hippocampal excitability. BMC Biol. *20*, 17. https://doi.org/10.1186/s12915-021-01203-0.
15. Manson, J.C., Hope, J., Clarke, A.R., Johnston, A., Black, C., and MacLeod, N. (1995). PrP gene dosage and long term potentiation. Neurodegeneration *4*, 113–114. https://doi.org/10.1006/neur.1995.0014.
16. Criado, J.R., Sánchez-Alavez, M., Conti, B., Giacchino, J.L., Wills, D.N., Henriksen, S.J., Race, R., Manson, J.C., Chesebro, B., and Oldstone, M.B.A. (2005). Mice devoid of prion protein have cognitive deficits that are rescued by reconstitution of PrP in neurons. Neurobiol. Dis. *19*, 255–265. https://doi.org/10.1016/j.nbd.2005.01.001.
17. Bhatt, Y., Hunt, D.M., and Carvalho, L.S. (2023). The origins of the full-field flash electroretinogram b-wave. Front. Mol. Neurosci. *16*, 1153934. https://doi.org/10.3389/fnmol.2023.1153934.
18. Masland, R.H. (2012). The neuronal organization of the retina. Neuron *76*, 266–280. https://doi.org/10.1016/j.neuron.2012.10.002.
19. Dmitriev, A.V., Dmitriev, A.A., and Linsenmeier, R.A. (2021). K(+)-dependent Muller cell-generated components of the electroretinogram. Vis. Neurosci. *38*, E010. https://doi.org/10.1017/S0952523821000092.
20. Lee, I.O., Skuse, D.H., Constable, P.A., Marmolejo-Ramos, F., Olsen, L.R., and Thompson, D.A. (2022). The electroretinogram b-wave amplitude: a differential physiological measure for Attention Deficit Hyperactivity Disorder and Autism Spectrum Disorder. J. Neurodev. Disord. *14*, 30. https://doi.org/10.1186/s11689-022-09440-2.
21. Encalada, S.E., Szpankowski, L., Xia, C.H., and Goldstein, L.S.B. (2011). Stable kinesin and dynein assemblies drive the axonal transport of mammalian prion protein vesicles. Cell *144*, 551–565. https://doi.org/10.1016/j.cell.2011.01.021.
22. Moser, T., Grabner, C.P., and Schmitz, F. (2020). Sensory Processing at Ribbon Synapses in the Retina and the Cochlea. Physiol. Rev. *100*, 103–144. https://doi.org/10.1152/physrev.00026.2018.
23. Kovermann, P., Engels, M., Müller, F., and Fahlke, C. (2021). Cellular Physiology and Pathophysiology of EAAT Anion Channels. Front. Cell. Neurosci. *15*, 815279. https://doi.org/10.3389/fncel.2021.815279.
24. Yoo, K.S., Lee, K., Oh, J.Y., Lee, H., Park, H., Park, Y.S., and Kim, H.K. (2019). Postsynaptic density protein 95 (PSD-95) is transported by KIF5 to dendritic regions. Mol. Brain *12*, 97. https://doi.org/10.1186/s13041-019-0520-x.
25. Vila, A., Shihabeddin, E., Zhang, Z., Santhanam, A., Ribelayga, C.P., and O'Brien, J. (2021). Synaptic Scaffolds, Ion Channels and Polyamines in Mouse Photoreceptor Synapses: Anatomy of a Signaling Complex. Front. Cell. Neurosci. *15*, 667046. https://doi.org/10.3389/fncel.2021.667046.
26. Tse, D.Y., Chung, I., and Wu, S.M. (2014). Pharmacological inhibitions of glutamate transporters EAAT1 and EAAT2 compromise glutamate transport in photoreceptor to ON-bipolar cell synapses. Vision Res. *103*, 49–62. https://doi.org/10.1016/j.visres.2014.07.020.
27. Lorenz, L., Hirmer, S., Schmalen, A., Hauck, S.M., and Deeg, C.A. (2021). Cell Surface

Profiling of Retinal Muller Glial Cells Reveals Association to Immune Pathways after LPS Stimulation. Cells *10*, 711. https://doi.org/10.3390/cells10030711.

28. Galindo-Romero, C., Norte-Muñoz, M., Gallego-Ortega, A., Rodríguez-Ramírez, K.T., Lucas-Ruiz, F., González-Riquelme, M.J., Vidal-Sanz, M., and Agudo-Barriuso, M. (2022). The retina of the lab rat: focus on retinal ganglion cells and photoreceptors. Front. Neuroanat. *16*, 994890. https://doi.org/10.3389/fnana.2022.994890.
29. Ioshimoto, G.L., Camargo, A.A., Liber, A.M.P., Nagy, B.V., Damico, F.M., and Ventura, D.F. (2018). Comparison between albino and pigmented rabbit ERGs. Doc. Ophthalmol. *136*, 113–123. https://doi.org/10.1007/s10633-018-9628-z.
30. Heiduschka, P., and Schraermeyer, U. (2008). Comparison of visual function in pigmented and albino rats by electroretinography and visual evoked potentials. Graefes Arch. Clin. Exp. Ophthalmol. *246*, 1559–1573. https://doi.org/10.1007/s00417-008-0895-3.
31. Rufiange, M., Dassa, J., Dembinska, O., Koenekoop, R.K., Little, J.M., Polomeno, R.C., Dumont, M., Chemtob, S., and Lachapelle, P. (2003). The photopic ERG luminance-response function (photopic hill): method of analysis and clinical application. Vision Res. *43*, 1405–1412. https://doi.org/10.1016/s0042-6989(03)00118-4.
32. Toomey, C.B., Kelly, U., Saban, D.R., and Bowes Rickman, C. (2015). Regulation of age-related macular degeneration-like pathology by complement factor H. Proc. Natl. Acad. Sci. USA *112*, E3040–E3049. https://doi.org/10.1073/pnas.1424391112.
33. Herrmann, R., Lobanova, E.S., Hammond, T., Kessler, C., Burns, M.E., Frishman, L.J., and Arshavsky, V.Y. (2010). Phosducin regulates transmission at the photoreceptor-to-ON-bipolar cell synapse. J. Neurosci. *30*, 3239–3253. https://doi.org/10.1523/JNEUROSCI.4775-09.2010.
34. Tanimoto, N., Sothilingam, V., Kondo, M., Biel, M., Humphries, P., and Seeliger, M.W. (2015). Electroretinographic assessment of rod- and cone-mediated bipolar cell pathways using flicker stimuli in mice. Sci. Rep. *5*, 10731. https://doi.org/10.1038/srep10731.
35. Pinto, L.H., Invergo, B., Shimomura, K., Takahashi, J.S., and Troy, J.B. (2007). Interpretation of the mouse electroretinogram. Doc. Ophthalmol. *115*, 127–136. https://doi.org/10.1007/s10633-007-9064-y.
36. Sato, S., Omori, Y., Katoh, K., Kondo, M., Kanagawa, M., Miyata, K., Funabiki, K., Koyasu, T., Kajimura, N., Miyoshi, T., et al. (2008). Pikachurin, a dystroglycan ligand, is essential for photoreceptor ribbon synapse formation. Nat. Neurosci. *11*, 923–931. https://doi.org/10.1038/nn.2160.
37. Wassle, H., Yamashita, M., Greferath, U., Grunert, U., and Muller, F. (1991). The rod bipolar cell of the mammalian retina. Vis. Neurosci. *7*, 99–112. https://doi.org/10.1017/s095252380001097x.
38. Striebel, J.F., Race, B., Leung, J.M., Schwartz, C., and Chesebro, B. (2021). Prion-induced photoreceptor degeneration begins with misfolded prion protein accumulation in cones at two distinct sites: cilia and ribbon synapses. Acta Neuropathol. Commun. *9*, 17. https://doi.org/10.1186/s40478-021-01120-x.
39. Carter-Dawson, L.D., and LaVail, M.M. (1979). Rods and cones in the mouse retina. I. Structural analysis using light and electron microscopy. J. Comp. Neurol. *188*, 245–262. https://doi.org/10.1002/cne.901880204.
40. Vinberg, F., Abbas, F., Choi, E.H., Tabaka, M., Seemab, U., Palczewski, K., and Leinonen, H.O. (2022). Upregulation of Rod Ribbon Synapse Components Coincides with Well-preserved Scotopic Vision in the P23H Model of Retinitis Pigmentosa. Invest Ophth Vis Sci *63*, 2695.
41. Sarria, I., Cao, Y., Wang, Y., Ingram, N.T., Orlandi, C., Kamasawa, N., Kolesnikov, A.V., Pahlberg, J., Kefalov, V.J., Sampath, A.P., and Martemyanov, K.A. (2018). LRIT1 Modulates Adaptive Changes in Synaptic Communication of Cone Photoreceptors. Cell Rep. *22*, 3562–3573. https://doi.org/10.1016/j.celrep.2018.03.008.
42. Frigg, R., Wenzel, A., Samardzija, M., Oesch, B., Wariwoda, H., Navarini, A.A., Seeliger, M.W., Tanimoto, N., Remé, C., and Grimm, C. (2006). The prion protein is neuroprotective against retinal degeneration in vivo. Exp. Eye Res. *83*, 1350–1358. https://doi.org/10.1016/j.exer.2006.07.010.
43. Ashok, A., Kang, M.H., Wise, A.S., Pattabiraman, P., Johnson, W.M., Lonigro, M., Ravikumar, R., Rhee, D.J., and Singh, N. (2019). Prion protein modulates endothelial to mesenchyme-like transition in trabecular meshwork cells: Implications for primary open angle glaucoma. Sci. Rep. *9*, 13090. https://doi.org/10.1038/s41598-019-49482-6.
44. Wilsey, L.J., and Fortune, B. (2016). Electroretinography in glaucoma diagnosis. Curr. Opin. Ophthalmol. *27*, 118–124. https://doi.org/10.1097/ICU.0000000000000241.
45. Yang, L., Wei, M., Xing, B., and Zhang, C. (2023). Extracellular matrix and synapse formation. Biosci. Rep. *43*, BSR20212411. https://doi.org/10.1042/BSR20212411.
46. Saha, S., Anilkumar, A.A., and Mayor, S. (2016). GPI-anchored protein organization and dynamics at the cell surface. J. Lipid Res. *57*, 159–175. https://doi.org/10.1194/jlr.R062885.
47. Linden, R. (2017). The Biological Function of the Prion Protein: A Cell Surface Scaffold of Signaling Modules. Front. Mol. Neurosci. *10*, 77. https://doi.org/10.3389/fnmol.2017.00077.
48. Le Pichon, C.E., Valley, M.T., Polymenidou, M., Chesler, A.T., Sagdullaev, B.T., Aguzzi, A., and Firestein, S. (2009). Olfactory behavior and physiology are disrupted in prion protein knockout mice. Nat. Neurosci. *12*, 60–69. https://doi.org/10.1038/nn.2238.
49. Spielhaupter, C., and Schätzl, H.M. (2001). PrPC directly interacts with proteins involved in signaling pathways. J. Biol. Chem. *276*, 44604–44612. https://doi.org/10.1074/jbc.M103289200.
50. Beckman, D., Santos, L.E., Americo, T.A., Ledo, J.H., de Mello, F.G., and Linden, R. (2015). Prion Protein Modulates Monoaminergic Systems and Depressive-like Behavior in Mice. J. Biol. Chem. *290*, 20488–20498. https://doi.org/10.1074/jbc.M115.666156.
51. Hasan, N., Pangeni, G., Cobb, C.A., Ray, T.A., Nettesheim, E.R., Ertel, K.J., Lipinski, D.M., McCall, M.A., and Gregg, R.G. (2019). Presynaptic Expression of LRIT3 Transsynaptically Organizes the Postsynaptic Glutamate Signaling Complex Containing TRPM1. Cell Rep. *27*, 3107–3116.e3. https://doi.org/10.1016/j.celrep.2019.05.056.
52. Cao, Y., Fajardo, D., Guerrero-Given, D., Samuel, M.A., Ohtsuka, T., Boye, S.E., Kamasawa, N., and Martemyanov, K.A. (2022). Post-developmental plasticity of the primary rod pathway allows restoration of visually guided behaviors. Curr. Biol. *32*, 4783–4796.e3. https://doi.org/10.1016/j.cub.2022.09.016.
53. Cao, Y., Wang, Y., Dunn, H.A., Orlandi, C., Shultz, N., Kamasawa, N., Fitzpatrick, D., Li, W., Zeitz, C., Hauswirth, W., and Martemyanov, K.A. (2020). Interplay between cell-adhesion molecules governs synaptic wiring of cone photoreceptors. Proc. Natl. Acad. Sci. USA *117*, 23914–23924. https://doi.org/10.1073/pnas.2009940117.
54. Hasan, N., and Gregg, R.G. (2024). Cone Synaptic function is modulated by the leucine rich repeat (LRR) adhesion molecule LRFN2. eNeuro *11*, ENEURO.0120-23.2024. https://doi.org/10.1523/ENEURO.0120-23.2024.
55. Gregg, R.G., Kamermans, M., Klooster, J., Lukasiewicz, P.D., Peachey, N.S., Vessey, K.A., and McCall, M.A. (2007). Nyctalopin expression in retinal bipolar cells restores visual function in a mouse model of complete X-linked congenital stationary night blindness. J. Neurophysiol. *98*, 3023–3033. https://doi.org/10.1152/jn.00608.2007.
56. Ueno, A., Omori, Y., Sugita, Y., Watanabe, S., Chaya, T., Kozuka, T., Kon, T., Yoshida, S., Matsushita, K., Kuwahara, R., et al. (2018). Lrit1, a Retinal Transmembrane Protein, Regulates Selective Synapse Formation in Cone Photoreceptor Cells and Visual Acuity. Cell Rep. *22*, 3548–3561. https://doi.org/10.1016/j.celrep.2018.03.007.
57. Um, J.W., and Ko, J. (2017). Neural Glycosylphosphatidylinositol-Anchored Proteins in Synaptic Specification. Trends Cell Biol. *27*, 931–945. https://doi.org/10.1016/j.tcb.2017.06.007.
58. Raymond, G.J., Zhao, H.T., Race, B., Raymond, L.D., Williams, K., Swayze, E.E., Graffam, S., Le, J., Caron, T., Stathopoulos, J., et al. (2019). Antisense oligonucleotides extend survival of prion-infected mice. JCI Insight *5*, e131175. https://doi.org/10.1172/jci.insight.131175.
59. Minikel, E.V., Zhao, H.T., Le, J., O'Moore, J., Pitstick, R., Graffam, S., Carlson, G.A., Kavanaugh, M.P., Kriz, J., Kim, J.B., et al. (2020). Prion protein lowering is a disease-modifying therapy across prion disease stages, strains and endpoints. Nucleic Acids Res. *48*, 10615–10631. https://doi.org/10.1093/nar/gkaa616.
60. Mortberg, M.A., Zhao, H.T., Reidenbach, A.G., Gentile, J.E., Kuhn, E., O'Moore, J., Dooley, P.M., Connors, T.R., Mazur, C., Allen, S.W., et al. (2022). Regional variability and genotypic and pharmacodynamic effects on PrP concentration in the CNS. JCI Insight *7*, e156532. https://doi.org/10.1172/jci.insight.156532.
61. Vallabh, S.M., Zou, D., Pitstick, R., O'Moore, J., Peters, J., Silvius, D., Kriz, J., Jackson, W.S., Carlson, G.A., Minikel, E.V., and Cabin, D.E. (2023). Therapeutic Trial of anle138b in Mouse Models of Genetic Prion Disease. J. Virol. *97*, e0167222. https://doi.org/10.1128/jvi.01672-22.
62. Wu, H., Kirita, Y., Donnelly, E.L., and Humphreys, B.D. (2019). Advantages of Single-Nucleus over Single-Cell RNA Sequencing of Adult Kidney: Rare Cell Types and Novel Cell States Revealed in Fibrosis. J. Am. Soc. Nephrol. *30*, 23–32. https://doi.org/10.1681/ASN.2018090912.
63. Wen, F., Tang, X., Xu, L., and Qu, H. (2022). Comparison of single-nucleus and single-cell

transcriptomes in hepatocellular carcinoma tissue. Mol. Med. Rep. *26*, 339. https://doi.org/10.3892/mmr.2022.12855.

64. Mironov, A., Jr., Latawiec, D., Wille, H., Bouzamondo-Bernstein, E., Legname, G., Williamson, R.A., Burton, D., DeArmond, S.J., Prusiner, S.B., and Peters, P.J. (2003). Cytosolic prion protein in neurons. J. Neurosci. *23*, 7183–7193. https://doi.org/10.1523/JNEUROSCI.23-18-07183.2003.
65. Fournier, J.G. (2008). Cellular prion protein electron microscopy: attempts/limits and clues to a synaptic trait. Implications in neurodegeneration process. Cell Tissue Res. *332*, 1–11. https://doi.org/10.1007/s00441-007-0565-5.
66. Matsunaga, Y., Peretz, D., Williamson, A., Burton, D., Mehlhorn, I., Groth, D., Cohen, F.E., Prusiner, S.B., and Baldwin, M.A. (2001). Cryptic epitopes in N-terminally truncated prion protein are exposed in the full-length molecule: dependence of conformation on pH. Proteins *44*, 110–118.
67. Mattapallil, M.J., Wawrousek, E.F., Chan, C.C., Zhao, H., Roychoudhury, J., Ferguson, T.A., and Caspi, R.R. (2012). The Rd8 mutation of the Crb1 gene is present in vendor lines of C57BL/6N mice and embryonic stem cells, and confounds ocular induced mutant phenotypes. Invest. Ophthalmol. Vis. Sci. *53*, 2921–2927. https://doi.org/10.1167/iovs.12-9662.
68. Mazzoni, F., Tombo, T., and Finnemann, S.C. (2019). No Difference Between Age-Matched Male and Female C57BL/6J Mice in Photopic and Scotopic Electroretinogram a- and b-Wave Amplitudes or in Peak Diurnal Outer Segment Phagocytosis by the Retinal Pigment Epithelium. Adv. Exp. Med. Biol. *1185*, 507–511. https://doi.org/10.1007/978-3-030-27378-1_83.

STAR★METHODS

KEY RESOURCES TABLE

REAGENT or RESOURCE	SOURCE	IDENTIFIER
Antibodies		
D13-anti prion protein (Human) 1:100	Matsuanaga[66]	N/A
Anti-Cone Arrestin - Arrestin 3/Cone photoreceptors – Rabbit - 1:100	Millipore	AB15282; RRID:AB_1163387
Anti-CtBP2 - C-terminal binding protein 2/ribeye protein of ribbon synapses - Mouse 1:100	Santa Cruz	sc-17759; RRID:AB_627310
Anti-PKCα - Protein kinase C/Rod bipolar cells - Goat 1:100	RD Systems	AF5340; RRID:AB_2168552
Anti -Pikachurin (ribbon synaptic cleft) - Rabbit 1:100	Proteintech	14578-1-AP; RRID:AB_2277653
Anti- EAAT1 - Excitatory amino acid transporter - Rabbit 1 1:100	Abcam	ab416; RRID:AB_304334
Anti-EAAT5 - Excitatory amino acid transporter 5 - Rabbit 1:100	Abcam	ab230217
Anti -PSD-95 - Post synaptic density-95 - Mouse 1:100	Neuromics	MO50000
Anti-Calbindin – horizontal cells – Rabbit 1:100	Abcam	Ab108404; RRID:AB_10861236
Critical commercial assays		
Chromium Next GEM Single Cell 3' Reagent Kits v3.1	10X Genomics	v3.1
A Nuclei PURE Prep Nuclei Isolation Kit	Sigma-Aldrich	Cat. # NUC-201
Deposited data		
snRNAseq Retina raw data-Striebel et al. 2024	This study	GEO accession: GSE264257
Experimental models: Organisms/strains		
C57BL/6J - *Prnp* $^{ZH3/ZH3}$ PrPKO mice	Adriano Aguzzi	University of Zurich
C57BL/6J mice	Jackson Laboratories, Bar Harbor, MA, USA	RRID:IMSR_ JAX:000664
Prnp $^{Edbg/Edbg}$ – PrPKO and WT - on 129/OlaP2Hsd mouse Background	Jean Manson - University of Edinburgh, Edinburgh, Scotland, UK	N/A
Oligonucleotides		
rd1 (Pde6B-1), rd2 (Prph2-1), rd8 (crb1.mut) and rd10 (Pde6b-3)	Transnetyx, Inc.– genotyping service	Cordova, TN
Software and algorithms		
Imaris x86_64 v.9.9.1 – confocal dataset analysis	This paper	Bitplane AG
GraphPad Prism 9.3.1	This paper	GraphPad
Huygens Professional v. 22.10 – deconvolution of confocal datasets	This paper	Scientific Volume Imaging
CellSens software – image acquisition and analysis	This paper	Olympus
ZEN v.2.3 software – confocal dataset acquisition	This paper	Carl Zeiss Microscopy
Espion V6 software – ERG data analysis	This paper	Diagnosys
Micron InSight OCT software OR) – quantification of retinal layer thickness.	This paper	Phoenix-Micron, Bend, OR).
Cell Ranger (version 6.0)	This paper	10X Genomics

EXPERIMENTAL MODEL AND STUDY PARTICIPANT DETAILS

Mice

The following mice were studied: C57BL/6J - *Prnp* $^{ZH3/ZH3}$ PrPKO mice provided by A. Aguzzi (University of Zurich, Zurich, Switzerland) via Mark Zabel (Colorado State University, Fort Collins, CO, USA)[11]; C57BL/6J mice obtained from Jackson Laboratories (Bar Harbor, Maine, USA) (RRID:IMSR_JAX:000664); *Prnp* $^{Edbg/Edbg}$ – PrPKO mice on a pure 129/Ola background and co-isogenic WT 129/Ola mice, both kindly provided by Jean Manson (University of Edinburgh, Edinburgh, Scotland, UK) and bred >10 generations at Rocky Mountain Laboratories (RML) (Hamilton, MT, USA). The "129/Ola" mouse name is a simplified nomenclature, officially they are designated as 129P2/OlaHsd and are white-bellied, pink-eyed (unpigmented), and have light chinchilla coat color.

Animals for ERG experiments were bred at RML to obtain adequate numbers for experimentation and then shipped to the Duke University School of Medicine (Durham, NC, USA), where they were maintained prior to experimentation in temperature and light (12 h light/12 h dark) controlled, hygenic rooms with food/water *ad libitum*. Ages of mice used in ERG experiments were; 129/Ola PrPKO (144–200 days old), 129/Ola (151–178 days old), C57BL/6J -PrPKO (151–186 days old) and C57BL/6J (158–165 days old). Details on sex and number of animals used are under the Optical Coherence Tomography section and in figure legends. Animals used for tissues for immunohistochemistry, immunofluorescence, confocal microscopy or snRNAseq experiments were group housed at RML, in transparent cages in a 12 h light (250–300 lx)/12 h dark cycle, and food and water were available ad libitium.

Ethics statement

All mice were housed at the Rocky Mountain Laboratories (RML) in an AAALAC-accredited facility in compliance with guidelines provided by the Guide for the Care and Use of Laboratory Animals (Institute for Laboratory Animal Research Council). Experimentation followed RML Animal Care and Use Committee an approved protocol (#2022–045). Mice were also housed and maintained at Duke University for ERG analyses, fundus imaging, and Optical Coherence Tomography (OCT) imaging, in accordance with the Institutional Animal Care and Use Committee at Duke University under an approved protocol (#A075-21-03) in adherence with the ARVO Statement for the Use of Animals in Ophthalmic and Vision Research.

METHOD DETAILS

Immunohistochemistry and immunofluorescence

To prepare for immunohistochemistry and immunofluorescence, eyes were removed, placed in 10% neutral buffered formalin for 3 to 5 days and then processed by dehydration and embedded in paraffin as a single block. 5 μm sections were then cut using a standard Leica microtome, placed on positively charged glass slides, and air-dried overnight at room temperature. The following day slides were heated in an oven at 60°C for 20 min. An automated Ventana Discovery XT stainer was used for deparaffinization, antigen retrieval and immunohistochemical staining.

For immunohistochemical staining of PrP^C, antigens were exposed by incubation in CC1 buffer (Ventana) containing Tris–Borate-EDTA, pH 8.0 for 100 min at 95°C. Staining for PrP^C was done using human anti-PrP monoclonal antibody D13[66] which was obtained from tissue culture supernatants made in our laboratory from CHO cells expressing the D13 antibody construct, which were kindly provided by Dr. R. Anthony Williamson, The Scripps Research Institute, La Jolla, CA. D13 culture fluid was used at a dilution of 1:100 (diluted in PBS with 1% normal goat serum and 0.1% Triton X-100) for 2 h at 37°C. The secondary antibody was biotinylated goat anti-human IgG at 1:500 dilution (Jackson ImmunoResearch, West Grove, PA.), and avidin-horseradish peroxidase was used with DAB as chromogen (DAB Map kit; Ventana Medical Systems, Tucson, AZ.).

For immunofluorescent staining, antigen retrieval for all targets was performed using a BioCare Medical DC2002 Decloaking chamber with sodium citrate buffer at pH 6.0(0.01 M) for 20 min at 120°C/20 PSI and cooled to 50°C. For each of the following steps, 250–300 μL of solution was applied to each slide and covered with a temporary plastic coverslip and incubated for a set amount of time. Tissues were blocked first with a normal donkey serum blocking solution (2% donkey serum, 1% BSA, 0.1% Triton X-100, 0.05% Tween 20 in 0.01 M PBS) for 1 h at room temperature and then in 0.1 M Glycine in 0.01 M PBS for 30 min at room temperature. Primary antibodies (see key resources table.) were diluted in donkey serum blocking solution and applied for 1 h at room temperature. AlexaFluor (ThermoFisher) secondary antibodies (AF-488, AF-568, AF-633/IgG (H + L) Cross-adsorbed secondaries, species-specific to primary antibodies) were diluted to 1:250 in donkey serum solution and applied for 1 h. In dual or triple stainings, primary antibodies were applied simultaneously, as were secondary antibodies. After each antibody incubation, slides were washed 3 times in 1X PBS for 10 min. Coverslips were mounted with ProLong Gold with DAPI (Cat. #P36931, Life Technologies) and dried overnight. Then slides were examined and photographed using an Olympus BX51 microscope/Olympus CellSens software or using a confocal microscope as described below.

Retinal nuclei isolation for single nucleus RNA sequencing

After enucleation of eyes, retinas were removed by dissection. The eyes were transferred to a culture dish and under a dissection microscope, the anterior part of the eye was removed with a circular cut at the *ora serrata*. The lens, iris and optic nerve were removed and using microforceps, light pressure was applied to the posterior area of the sclera until the retina separated from the retinal pigmented epithelium (RPE) and sclera. Retinas were gently peeled away and transferred to ice-cold PBS. Four retinas were pooled, from two female mice, on two separate occasions for analysis (for this study, $n = 4$ mice or $n = 8$ retinas). A Nuclei PURE Prep Nuclei Isolation Kit (Sigma – Cat. # NUC-201) was used with modifications as described. Briefly, cold PBS was removed from retinas and exchanged with Lysis Buffer (250 μL/retina), incubated on ice for 15 min, swirled 2–3 times during incubation. After the 15-min incubation the retinas were triturated lightly with a 5mL serological pipette to break into large chunks. If present, pieces of black ciliary or retinal pigmented epithelium were removed with a 1mL pipette. Next, the semi-homogenate was triturated 10–15 times with a silanized Pasteur pipette. The homogenate was then applied to a 30μm Milteyi MACS Smartstrainer to remove cellular debris and large clumps. The flow through was then centrifuged at 1000 *g* for 10 min at 4.0°C. Supernatant was then removed without disrupting the pellet of nuclei. 5mL of Nuclei Wash and Resuspension buffer from Sigma Kit was added and pellet was resuspended with a 5mL serological pipette. The mixture was then centrifuged at 1000 *g* for 10 min at 4.0°C, again supernatant was removed,

and pellet was resuspended in Nuclei Wash and Resuspension buffer. Nuclei were counted in a hemacytometer and used for 10x Genomics RNAseq analysis as below. Other steps in the Sigma protocol were not utilized for retinal lysates.

Single nuclei RNA library construction and next-generation sequencing

Single nuclei suspensions were obtained from retina as described above. 8,000 nuclei per retina pool were loaded on a 10X Genomics Next GEM chip and single-nuclei GEMs were generated on a 10X Chromium Controller. Subsequent steps to generate cDNA and sequencing libraries were performed following 10X Genomics' protocol using the Chromium Next GEM Single Cell 3' Reagent Kits v3.1. Libraries were pooled and sequenced using Illumina NovaSeq S2 with NextSeq 100 to 300 cycle kits as per 10X sequencing recommendations. The sequenced data were processed using Cell Ranger (version 6.0) to demultiplex the libraries. The reads were aligned to *Mus musculus* genome (cellranger-mm10–1.2.0) to generate count tables which were combined into a single feature-barcode matrix allowing the data to be further analyzed using 10X Genomics Loupe Browser. Extensive details of library construction protocol can be found in the 10X Genomics Next GEM protocol (Chromium Single Cell 3′ Reagent Kits User Guide (v3.1 Chemistry, https://www.10xgenomics.com/support/single-cell-gene-expression/documentation/steps/library-prep/chromium-single-cell-3-reagent-kits-user-guide-v-3-1-chemistry).

Dataset is available at GEO accession: GSE264257.

Confocal microscopy

Samples were imaged using a Zeiss laser scanning confocal (LSM 880) microscope driven by ZEN v.2.3 software (Carl Zeiss Microscopy). A Plan Apochromat 63X/NA1.4 oil immersion lens was used, with immersion oil at a refractive index of 1.518. Image acquisition settings including laser power and gain were optimized for minimal background and crosstalk, and kept constant within an experiment for all timepoints and samples to enable direct comparisons. Stacks were collected with a lateral resolution of 35 nm and z-spacing of 260 nm.

Confocal image processing and analysis

Image stacks were exported from ZEN software and deconvolved with Huygens Professional v. 22.10 (Scientific Volume Imaging, The Netherlands) using the CMLE algorithm, with SNR = 20 and a maximum of 40 iterations. The deconvolved datasets were imported to Imaris x86_64 v.9.9.1 (Bitplane AG, Zürich, Switzerland) for visualization and analysis.

Electron microscopy sample preparation

C57BL/10SnJ mice were perfused with 2% paraformaldehyde +2% glutaraldehyde in 0.1 M Sorensen's phosphate buffer (Electron Microscopy Sciences, Pennsylvania). Eyes were enucleated and placed in fresh fixative for at least 30 min before further processing. The anterior portions of eyes were dissected and discarded. The remaining posterior eye cups were rinsed in phosphate buffer, followed by embedment in 2.5% low-melt agar (Precisionary, Massachusetts) made in PBS. 200 μm sections were cut with a VT1000S vibrating blade microtome (Leica Biosystems, Illinois). Sections were processed for transmission electron microscopy as follows: postfixation with 0.05% osmium tetroxide +0.08% potassium ferrocyanide in 0.1 M phosphate buffer for 1 h, rinsed with buffer, then dehydrated in a graded ethanol series to 100%, infiltrated with LRWhite (Electron Microscopy Sciences, Pennsylvania) and polymerized overnight in homemade flat-embedding molds covered with aclar sheets at 50°C in a vacuum oven.

Transmission electron microscopy

Flat-embedded vibratome sections were excised and super-glued onto resin stubs such that ultramicrotomy sections would be in the desired orientation. 70 nm sections were cut with an Ultracut UCT (Leica Biosystems, Illinois) ultramicrotome and picked up on Formvar coated 100 hex mesh copper grids (Electron Microscopy Sciences, Pennsylvania). Micrographs were acquired on an HT7800 (Hitachi, Oregon) operating at 80 kV with an XR-81B CMOS digital camera (AMT Imaging Systems, Massachusetts).

Optical coherence tomography (OCT), fundus imaging and assessment for retinal degeneration genes

Using a Micron IV retina camera with OCT head unit (Phoenix-Micron, Bend, OR), multiple fundus and OCT images were taken of both eyes of each mouse to assess the layers of retina. Retinal OCT images were segmented and quantified using Micron InSight OCT software (Phoenix-Micron, Bend, OR). OCT imaging was found to be unremarkable in all mice, except 4 male 129/Ola PrPKO mice from one litter. These mice had variable levels of thinning of the photoreceptor layer (both outer nuclear and outer segment layers) of unknown causes. As a precaution, 129/Ola PrPKO and 129/Ola WT, males and females, were analyzed for the most common retinal degeneration mutations – rd1 (Pde6B-1), rd2 (Prph2-1), rd8 (crb1.mut) and rd10 (Pde6b-3). The C57BL/6J line does not carry the rd8 mutation,[67] but as a precaution a subset of C57BL/6J and ZH3PrPKO mice were nonetheless assessed for the rd1 and rd8 mutation. All strains tested negative for the presence of these retinal degeneration mutations. The decision was made to exclude all 6 male 129/Ola PrPKO and 6 WT mice, in case there was an unknown mutation sorting in the male mice. Data presented in the main paper includes 129/Ola females only, for this reason. Importantly, studies have shown no differences between male and female mice in ERG responses.[68] Data for C57BL/6J PrPKO and WT mice includes both males and females, no significant differences in were noted between male and female mice on the C57BL/6J background.

In vivo retinal function analysis by electroretinography (ERG)

ERG was in large part performed as previously described.[32] Briefly, mice were dark-adapted for at least 4 h, pupils dilated with 0.5% (w/v) tropicamide and 1.25% (w/v) phenylephrine and anesthetized with a mixture of ketamine (100 mg/kg) and xylazine (10 mg/kg). Scotopic and photopic ERG responses, were recorded using an Espion E3 ERG apparatus with a ColorDome flash simulator to provide binocular full-field ganzfeld stimulation (Diagnosys LLC, Lowell, MA), at increasing flash intensities under both scotopic and photopic (with a background light) conditions. Recordings consisted of single flash presentations, repeated 0–15 times to verify the response reliability and improve the signal-to-noise ratio, if required. For flicker responses, flashes were repeated 20–30 times. Low-pass frequency filtering of 50 Hz was applied to remove oscillatory potentials and noise, for acquisition of a-, b-, and c-waves. Details of light intensities, repeats, interval times, adaptation times, light color, response component, and cell types assessed, for all steps in the ERG analyses, are presented in Table S1.

Espion V6 software (Diagnosys) was used to organize and analyze ERG responses. Parameters analyzed included the amplitudes and implicit times (time to peak of wave) of; a-waves (photoreceptors), b-waves (bipolar and Müller), oscillatory potentials (amacrine cell, inner retinal cells) and photopic negative response (PhNR, retinal ganglion cells) were collected and analyzed. *p*-values for all comparisons made between wildtype mice and prion protein knockout mice are shown in Tables S2 and S3.

QUANTIFICATION AND STATISTICAL ANALYSIS

Statistical analysis of single nuclei RNA sequencing data in Figure 1, was conducted using Loupe Browser v6 software. Differential expression of genes between cell clusters in Figures 1 and S1 was determined by a negative binomial exact test (sSeq method) which is coded into the Loupe Browser software, details on this algorithm and code are available at https://kb.10xgenomics.com/hc/en-us. Details on snRNAseq sample preparation and n values are in the snRNAseq Methods section above. In Figure 1H, asterisks represent the following p-values *p<0.05. Here and in all figures *p* values less than 0.05 were deemed to be statistically significant. Statistical analysis in Figures 3, 4, 6, 7, S3, and S4 was performed using GraphPad Prism v9.3.1. In each of these figures non-parametric unpaired tests (Mann-Whitney) were used to compare data and asterisks represent the following *p*-values *$p < 0.05$, **$p < 0.01$, ***$p < 0.001$, ns, not significant. Information on the value of n, what n represents, definition of center and other statistical details can be found in the figure legends. Gender and number of animals used in ERG and OCT analyses are dicussed in detail under the Optical coherence tomography (OCT), fundus imaging and assessment for retinal degeneration genes section of Methods. Quantification of fluorescent images was performed using IMARIS software as described in figure legends.